FORSCHUNGSZENTRUM
ROSSENDORF e.V.

FZR

FZR-181
May 1997
Preprint

H.-G. Ortlepp, W. Wagner, C.-M. Herbach, A. A. Aleksandrov, I. A. Aleksandrova, M. Andrassy, A. Budzanowski, B. Czech, M. Danziger, L. Dietterle, V. N. Doronin, S. Dshemuchadse, A. S. Fomichev, W. D. Fromm, M. Gebhardt, P. Gippner, K. Heidel, Sh. Heinitz , H. Homeyer, S. A. Ivanovsky, D. V. Kamanin, I. V. Kolesov, A. Matthies, D. May, S. I. Merzlyakov, W. von Oertzen, Yu. Ts. Oganessian, G. Pausch, Yu. E. Penionzhkevich, Yu. V. Pyatkov, S.V. Radnev, G. Renz, L. A. Rubinskaya, I. D. Sandrev, K. D. Schilling, W. Seidel, D. I. Shishkin, A. P. Sirotin, H. Sodan, O. V. Strekalovsky, V. G. Tishchenko, V. V. Trofimov, I. P. Tsurin, C. Umlauf, D. V. Vakatov, V. M. Vasko, V. A. Vitenko, E. Will, M. Wilpert, R. Yanez, V. E. Zhuchko, P. Ziem, and L. Zrodlowski

The 4π - fragment - spectrometer FOBOS

Forschungszentrum Rossendorf e.V.
Postfach 51 01 19 · D-01314 Dresden
Bundesrepublik Deutschland

Telefon	**(+49) 351 / 260 2745**
Telefax	**(+49) 351 / 260 3700**
E-Mail	**wagner@fz-rossendorf.de**

The 4π - fragment - spectrometer FOBOS [$]

H.-G. Ortlepp [a, b], W. Wagner [a, b, *], C.-M. Herbach [a,b], A.A. Aleksandrov [b, d], I.A. Aleksandrova [b, d], M. Andrassy [a], A. Budzanowski [g], B. Czech [g], M. Danziger [h], L. Dietterle [a,b], V.N. Doronin [b], S. Dshemuchadse [a], A.S. Fomichev [b], W.D. Fromm [l], M. Gebhardt [k], P. Gippner [a,b], K. Heidel [a], Sh. Heinitz [a, b], H. Homeyer [e], S.A. Ivanovsky [b], D.V. Kamanin [a, b], I.V. Kolesov [b], A. Matthies [a, b], D. May [a, b], S.I. Merzlyakov [b], W. von Oertzen [f], Yu.Ts. Oganessian [b], G. Pausch [a], Yu.E. Penionzhkevich [b], Yu.V. Pyatkov [d], S.V. Radnev [c], G. Renz [a, b], L.A. Rubinskaya [b], I.D. Sandrev [c †], K.D. Schilling [a], W. Seidel [a], D.I. Shishkin [b], A.P. Sirotin [b], H. Sodan [l], O.V. Strekalovsky [b], V.G. Tishchenko [b], V.V. Trofimov [b], I.P. Tsurin [b], C. Umlauf [a, b], D.V. Vakatov [b], V.M. Vasko [b], V.A. Vitenko [i], E. Will [a], M. Wilpert [f], R. Yanez [a], V.E. Zhuchko [b], P. Ziem [e], and L. Zrodlowski [g]

[a] *Forschungszentrum Rossendorf e.V., 01314 Dresden, PF 510119, Germany*
[b] *Joint Institute for Nuclear Research, 141980 Dubna (Moscow region), Russia*
[c] *Laboratory for Technical Developments and Applications, Bulgarian Academy of Sciences, 1184 Sofia, Bulvar Zarigradsko Shose 72, Bulgaria*
[d] *Moscow Engineering Physics Institute, 115409 Moscow, Kashirskoye Shosse 31, Russia*
[e] *Hahn-Meitner-Institut GmbH, 14195 Berlin, Glienicker Str. 100, Germany*
[f] *Freie Universität Berlin, 14195 Berlin, Arnimallee 14, Germany*
[g] *Henryk Niewodniczansky Institute of Nuclear Physics, 31-342 Cracow, ul. Radzikowskiego 152, Poland*
[h] *Technische Universität Dresden, 01062 Dresden, Mommsenstr. 13, Germany*
[i] *Khlopin-Radium-Institute, St. Petersburg, ul. Rentgena 1, Russia*
[k] *Johann Wolfgang Goethe - Universität, 60054 Frankfurt am Main, PF 111932, Germany*
[l] *Zentralinstitut für Kernforschung (before 1992), Rossendorf, Germany*

Abstract

The 4π - fragment - spectrometer FOBOS developed for heavy-ion research at beam energies of 10 ÷100 AMeV has been commissioned for physical experiments at the Flerov Laboratory of Nuclear Reactions of the Joint Institute for Nuclear Research in Dubna. Based on the logarithmic detector principle, it is able to register charged fragments from protons up to heavy residual nuclei in a large dynamical range. Position-sensitive avalanche counters, axial ionization chambers and CsI(Tl) scintillation detectors are arranged in three concentric detector shells. An array of phoswich detectors is used as a more granular forward detector at narrow polar angles. The modular concept of FOBOS allows for different experimental application in the field of exclusive fragment spectroscopy at medium multiplicities. For illustration the fragment spectroscopy studies concerning the spontaneous fission process and the fragmentation of hot nuclei by means of the FOBOS set-up are considered.

[$] The FOBOS project has been supported by the BMBF, Germany, contract Nr.: 06 DR 100 and 06 DR 671.

[*] Corresponding author. Present address: Forschungszentrum Rossendorf e.V., Institut für Kern- und Hadronenphysik, D-01314 Dresden, PF 510119, Germany. Telephone: (+49) (351) 260 2745 Fax: (+49) (351) 260 3700
e-mail: WAGNER@FZ-ROSSENDORF.DE and WAGNER@NRSUN.JINR.DUBNA.SU

Contents

1. Introduction

2. FOBOS set-up

2.1 Mechanical design
2.2 Position-sensitive avalanche counters
2.3 Axial ionization chambers
2.4 Evacuation and gas-supply system
2.5 Scintillator shell
2.6 Forward array

3. Data acquisition system

3.1 First-level trigger
3.2 Read-out electronics
3.3 Experimental data structure
3.4 Data analysis software

4. Calibration procedures

4.1 Calibration of the parameters measured by the gas-filled detector modules

4.1.1 Calibration of the coordinates of the position-sensitive avalanche counters
4.1.2 Energy calibration of the Bragg chambers
4.1.3 Time calibration of the position-sensitive avalanche counters

4.2 Calibration of the scintillation detectors

5. Physical observables of charged particles

6. Experiments at FOBOS

6.1 Fragment spectroscopy of spontaneous fission
6.2 Fragmentation of hot nuclei

6.2.1 TKE - Mass distributions of binary fission of hot nuclei
6.2.2 Velocity analysis of ternary decays
6.2.3 The charged-particle clock

7. Summary

Acknowledgments

Tables

References

1. INTRODUCTION

The 4π-fragment-spectrometer FOBOS [1,2], the construction of which was first conceived in 1984 [3], with the aim to study heavy-ion induced reactions in the low- and intermediate-energy regions between 10 and 100 AMeV, is now regularly operating in its full configuration at the Flerov Laboratory of Nuclear Reactions (FLNR) of the Joint Institute for Nuclear Research (JINR) in Dubna.

FOBOS was originally planned to operate with the beams of the then proposed cyclotron-tandem facility [4]. Presently, it is nevertheless using the heavy-ion beams emanated from the isocronous cyclotron U-400M, recently equipped with an ECR ion-source [5], an arrangement which for ions up to about Xe provides nearly the same beam energies as those expected from the cyclotron-tandem concept [6]. By means of projectile fragmentation, radioactive secondary-ion beams also became possible. This opens new perspectives for heavy-ion research in the above mentioned energy region.

The spectrometer FOBOS is specially designed for reaction studies in direct kinematics, i.e., for reactions where a light projectile impinges upon a heavy target nucleus. For bombarding energies higher than about 20 AMeV, the complete fusion scenario changes over to an incomplete fusion mechanism, and therefore, the linear momentum transferred (LMT) to the compound-like system stays relatively moderate. Depending on mass, excitation energy (E*) and angular momentum, the decay of this complex system is mostly characterized by the emission of a fairly large number ($\approx 10 \div 30$) of neutrons, a medium number of light charged particles (LCPs), fission, yielding two fission fragments (FFs), and/or the emission of a small number of intermediate mass fragments (IMFs), conventionally defined as having masses between an α-particle and FFs. FOBOS is able to register charged reaction products only, ranging from protons up to heavy residues (HRs). The charged ejectiles resulting from the above mentioned decay patterns may be emitted in any direction in space. Therefore, a spherical detector design was conceived in order to cover most of the solid angle around the target, and consist of a 32 face truncated isocahedron in which 20 of the faces are regular hexagons and 12 are regular pentagons, respectively.

To perform exclusive spectroscopy of charged fragments over a broad dynamical range, covering large intervals of atomic number (Z), mass number (A) and solid angle ($\Delta\Omega$), requires reasonable compromise between registration efficiency, detector granularity, detection thresholds and counting rates. With this aim, the so-called logarithmic detection

principle is invoked, whereby a successive increase of stopping power along the flight path of the particles is performed by combining different detector types (mainly gas-filled and solid-state detectors). A spectrometer designed next to these lines often ends having a rather heterogeneous construction and, for technical reasons, seldom achieves full geometrical efficiency (4π).

In the particular case of the spectrometer FOBOS, the above principle is fulfilled by the combination of three consecutive shells of particle detectors and a more granular forward array. The inner detector shell, consisting of 30 position-sensitive avalanche counters (PSACs), and the relatively long flight path of 50 cm between the target and shell, provides the means for a very precise time-of-flight (TOF) and coordinate (X,Y) measurement of fragments with $Z \geq 2$. Furthermore, the TOF and pulse-height (ΔE) information of the PSACs makes possible a rough Z-identification of heavy species, e.g. HRs, not reaching the next detector shell.

The second detector shell, consisting of 30 axial Bragg ionization chambers (BICs), measures the stopping power of the fragments along their path within the gas volume (Bragg curve). The residual energy (E_R) and the magnitude of the Bragg-peak (BP), being a measure of the fragment charge (Z), are directly derived. From the TOF and the E_R information, the fragment masses (m_i) can be calculated by making suitable corrections to the energy losses in the penetrated detector materials. Adding to this the coordinate information, the momentum vectors (p_i) of each fragment can be derived "event by event" in an independent manner. This feature is a necessary condition for exclusive measurements.

For the detection of energetic LCPs ($Z = 1 \div 2$) a third, more granular, scintillator shell of CsI(Tl) detectors [7,8] is arranged behind the BICs. The PSACs and BICs are not sensitive to low ionizing fast LCPs and, consequently, the passage of these particles through these detectors does not affect the registration of other fragments. Therefore, independent correlations between fragments and energetic LCPs can be studied at all possible relative angles. The LCPs are analyzed by their signal pulse-height and -shape, and the well-known ΔE-E-method can be used for the identification of highly energetic IMFs that penetrate the BICs and are stopped in the scintillators.

Altogether, FOBOS is arranged in 30 separate detector modules, each consisting of one PSAC, one BIC, and a mosaic of 7 CsI(Tl) scintillation counters, in that order from the inside to the outside, and mounted in the regular hexagons and pentagons to face the central vacuum chamber. Two of the regular pentagons of the main construction are used for the

beam entrance and exit. A more granular concentric array of phoswich detectors (see section 2.6) is placed inside the central vacuum chamber covering forward angles of $\vartheta = 4.5^{o} \div 26^{o}$. Fig. 1 shows schematically the particle parameters that are either measured or derived from the signals delivered by a FOBOS module.

In the following chapters, the main elements of the spectrometer FOBOS are described in detail paying more attention to its original and advantageous features than to basic detection principles widely known from the literature. A few preliminary results, obtained with this new spectrometer in the first series of experiments during the period of commissioning, are mainly given for illustration of its properties.

It should be mentioned that a similar 4π-array for charged fragments is operating at the Cyclotron Laboratory of the Michigan State University, East Lansing, USA [9]. Its general concept resembles that of the spectrometer FOBOS, and several detection principles used in these two devices are almost identical. In spite of this, FOBOS has several advantageous features, which could be achieved thanks to various completely different technical solutions, due in particular to its three times longer flight path.

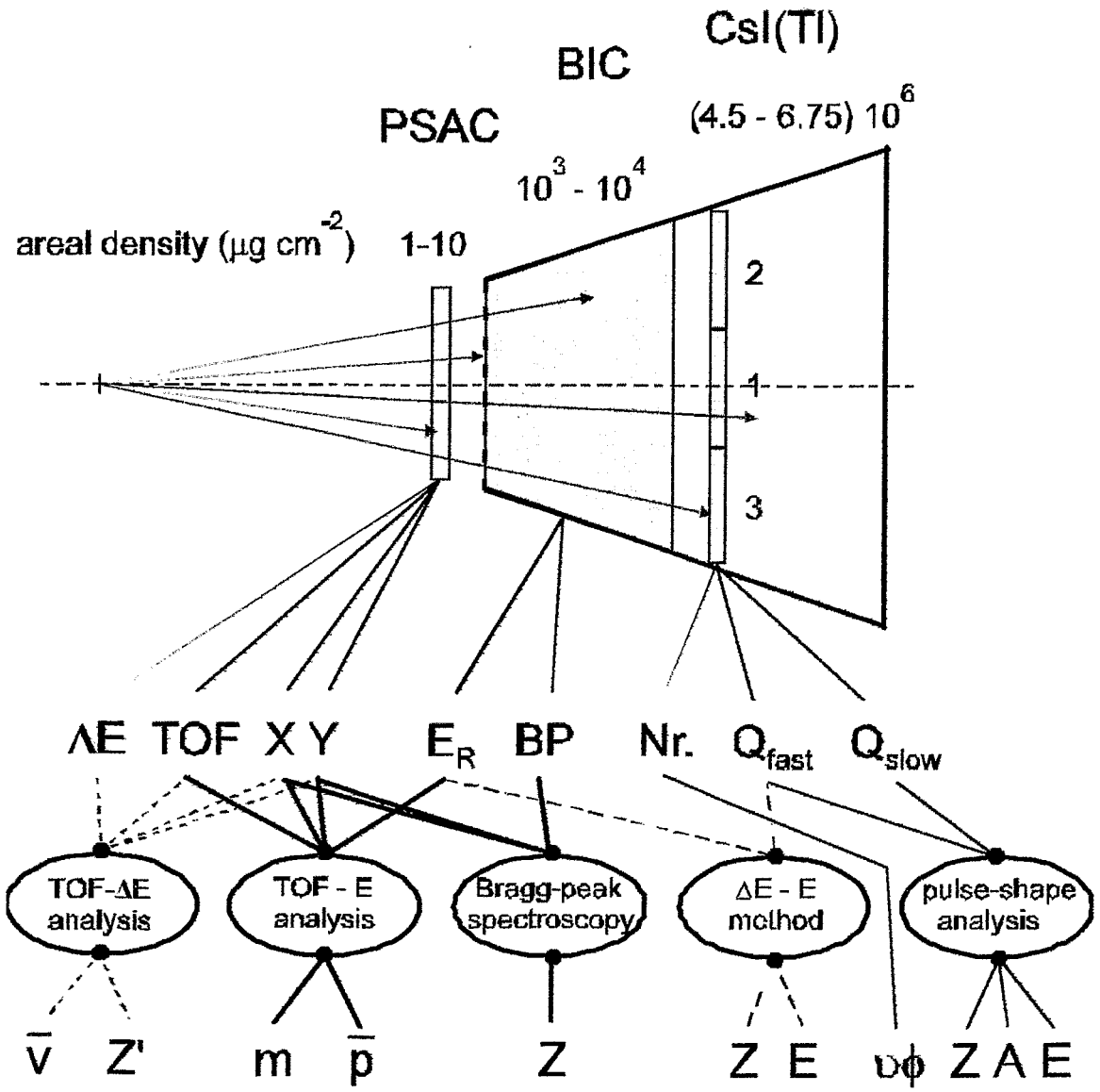

Fig. 1 Sketch of the parameters of charged particles, measured or derived from the signals delivered by a detector module. Different methods of analysis are applied, if

(i) only the PSAC has fired (dotted lines), (ii) the PSAC and BIC have fired (thick full lines),

(iii) only a CsI(Tl) detector (1,2,3, ... 7) has fired (thin full lines), and

(vi) the BIC and a CsI(Tl) detector have fired (dashed lines).

The logarithmically increasing stopping power of the different detector shells is illustrated by the given mean areal densities of the detector materials of the PSACs, BICs, and CsI(Tl) crystals for typical experimental conditions.

2. FOBOS SET-UP

2.1 Mechanical design

The general lay-out of the spectrometer FOBOS is schematically shown in fig. 2. The central vacuum chamber [10] is a monolithic hollow body with an inner diameter of 1330 mm. Viewed from the outside, the shape is a precisely manufactured (± 0.2 mm) 32-face truncated isocahedron with circular holes in the centers of the hexagonal (∅ = 480 mm) and pentagonal (∅ = 380 mm) surface elements, where the 20 large and 10 small detector modules are mounted. The angles (ϑ,φ) of the centers of the modules are given in tab. 1.

The entrance tube to FOBOS has an inner diameter of 300 mm. A cone of $\vartheta \approx 12^{\circ}$ at the beam exit can house a special forward array. Two carrier columns support the detector axis at both sides. The evacuation of the central volume is performed along the main axis. The vacuum connections to the beam line make possible the rotation of the fully mounted FOBOS device for changing the modules and performing other services.

The hexagonal- and pentagonal-shaped frames of the PSACs are mounted separately in front of the BIC entrance windows. Part of the mechanical structure of the BICs protrudes into the central vacuum chamber. The PSACs of the first detector shell also form a truncated isocahedron-like shape at a distance of about 50 cm from the target (fig. 2). Their sensitive areas are circles of diameters ∅ = 327 mm and ∅ = 243 mm for the large and small detector modules, respectively.

The conical-shaped BICs have apertures of 260.0 msr ($\Delta\vartheta = 33.08^{\circ}$) and 167.8 msr ($\Delta\vartheta = 26.54^{\circ}$), respectively. This results in a total solid angle of 7.1 sr (56.5 % of 4π) covered by the PSACs, and 6.88 sr (54.7 % of 4π) covered by the BICs.

The mosaics of 7 hexagonal-shaped CsI(Tl) crystals are positioned together with their light-guides and photomultipliers inside the BIC cases covering 84 % of the BIC aperture. Rubber rings pressed on the phototubes serve as seals between the gas volumes of the BICs and the atmosphere.

The forward array of 92 phoswich detectors, arranged in 6 concentric rings around the beam axis at distances of $10 \div 25$ cm from the target, covers an interval of polar angles between $\vartheta = 4.5^{\circ} \div 26.5^{\circ}$. It can be inserted into the central vacuum chamber through the exit cone. The outer ring of the forward array slightly overlaps with the BICs positioned in the forward direction at $<\vartheta> = 37.4^{\circ}$.

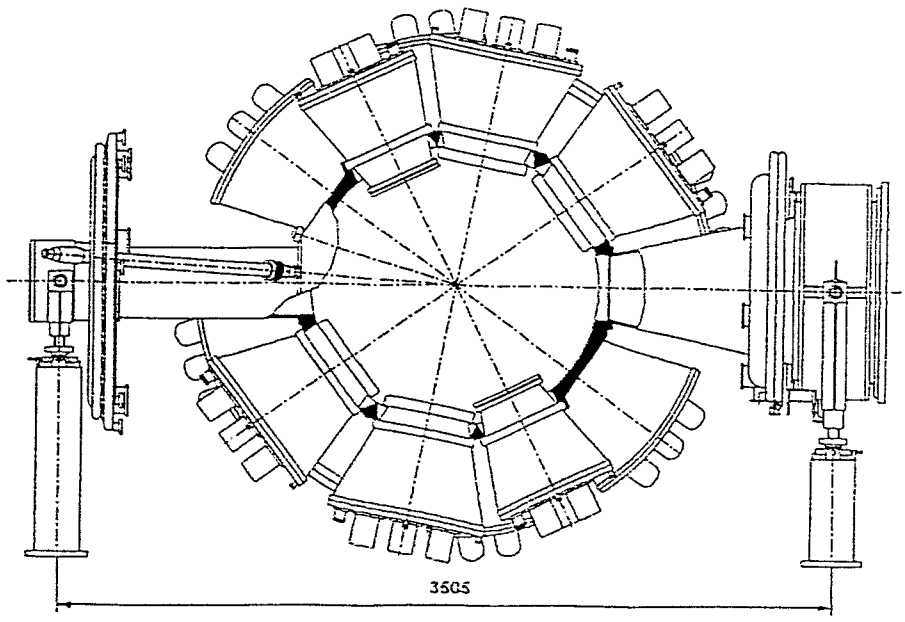

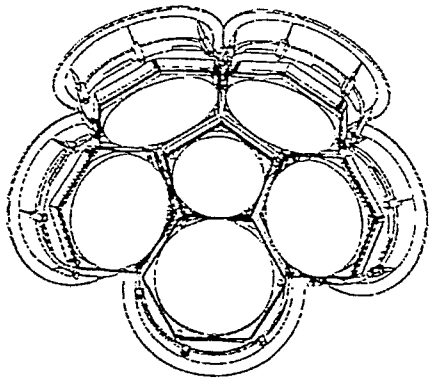

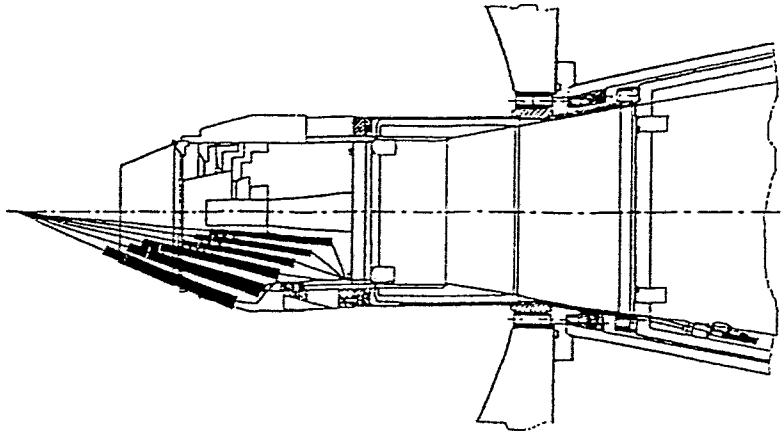

Fig. 2

Fig. 2 General lay-out of the FOBOS spectrometer. Cross-sectional view of the central vacuum chamber with mounted detector modules (upper part). The beam enters from the left side. The exit cone at the right side houses the forward array. A cross-sectional view of the forward array is shown in the lower part. (For more clearness only half of the phoswich detectors are drawn.) The mechanical arrangement of five large hexagonal PSACs surrounding one small pentagonal PSAC is shown in the central part. The circles define the sensitive areas of the PSAC.

2.2 Position - sensitive avalanche counters

The PSACs are based on the principles described in ref. [11]. Three thin Mylar foils (1.2 μm) are used as cathode and PSAC windows. The central cathode-foil is covered by 40 μg cm^{-2} thick Au layers and delivers the timing signal. Two perpendicular wire-planes (made of 30 μm thick Au-coated W, spaced by 1 mm) are positioned at a distance of 3 mm ± 50 μm on both sides of the common cathode. They serve as anode coordinate grids. The window foils are glued to special frames which can be changed individually in the case of gas leakage. The transparency of the PSAC amounts to 92 %.

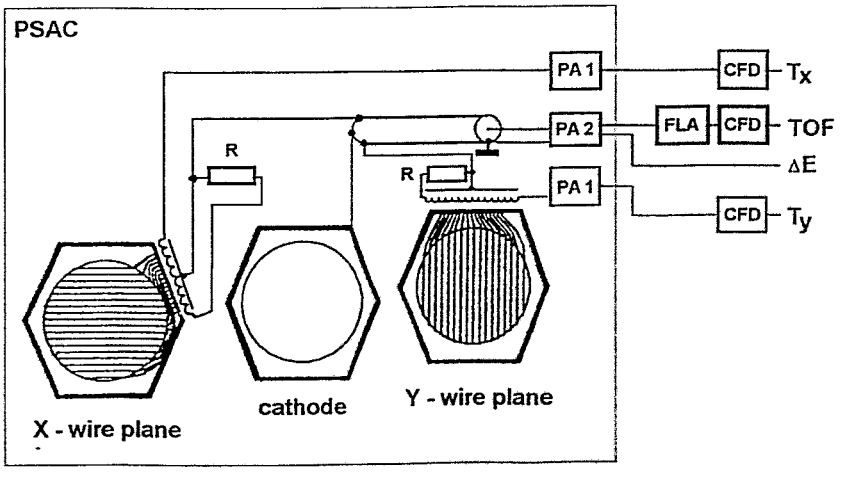

Fig. 3 Principal scheme of the PSAC read-out. Delay lines are capacitively coupled to the X- and Y- wire planes. Three preamplifiers (PA) for the coordinates and timing signals are directly mounted to the PSAC frame. A fast linear amplifier (FLA) for the timing signal (TOF) drives the long cable line to the front-end electronics in the measurement hall. A CAMAC module contains the three constant fraction discriminators (CFD).

Pairs of neighbouring coordinate wires are connected to conductive strips which are capacitively coupled to a wound read-out delay-line of 1.4 ns mm^{-1} specific delay and 560 Ω impedance. The delay lines of the two coordinate grids are matched with resistors at one end and coupled to special read-out amplifiers at the other end. The cathode read-out circuit delivers an amplified current signal for timing and a charge signal for pulse-height analysis. All electronic channels are protected against damage if spark discharges occur in the counters. The surface-mounted circuits and the delay lines are placed in non-sensitive areas directly inside the PSAC frames. The spatial resolution of the PSACs amounts to $\Delta x = \Delta y \approx 1.5$ mm. A principal scheme of the PSAC read-out is shown in fig. 3.

The counter gas is pentane at a pressure between 200 Pa and 800 Pa. The voltage (typically ≈ 500 V) is set about 5 V below the onset of spark discharges, which may be induced by feed-back effects after the passage of highly ionizing particles. This voltage level guarantees an effective registration of heavy fragments with a lower threshold of ≈ 0.05 AMeV. The efficiency of registration for α-particles drops for energies ≥ 1.5 AMeV because of the decreasing energy loss in the sensitive volume.

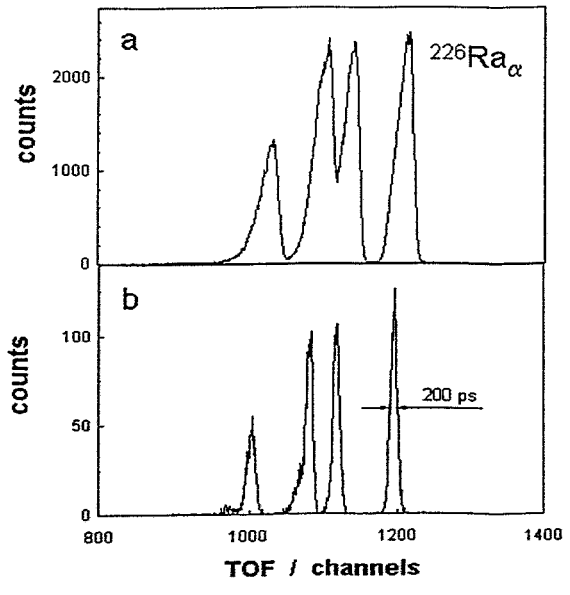

Fig. 4 Time-of-flight spectrum of a ^{226}Ra α-source measured by a PSAC against the timing reference signal of a small transmission avalanche counter. The energies of the α-lines are given in fig. 12.
Upper panel (a): irradiating the entire sensitive area; lower panel (b): irradiating only a small central part of the PSAC.
The time resolution is 200 ps.

By using a ^{226}Ra α-source, the time resolution of the PSAC is measured against a small parallel-plate avalanche counter which provides the START-signal for the TOF measurement. Fig. 4b shows a TOF spectrum where only a small central

area of the counter was irradiated. The FWHM amounts typically to ≈ 200 ps. Irradiation of the entire sensitive area of the PSAC (fig. 4a) worsen the resolution by a factor of about three. This is caused by the influence of electronic signal delays. Therefore, a map of calibrated TOF signals was created for each PSAC (fig. 5) which can be used for a coordinate-dependent correction of the measured TOF. With this procedure it is possible to reduce the coordinate dependence of the TOF with an accuracy of ≈ 100 ps.

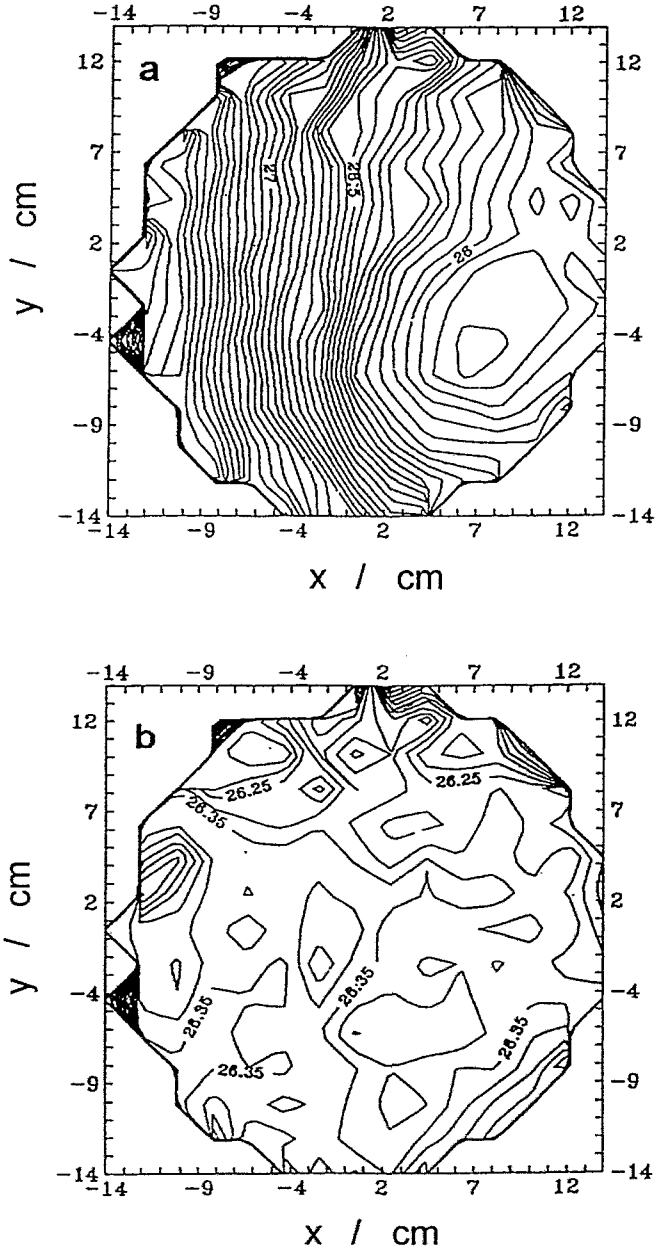

Fig. 5 Contour plots of calibrated time - of - flight signals of a PSAC with a step of 0.05 ns.
Upper panel (a): uncorrected; lower panel (b): corrected for the dependence on the PSAC coordinates.

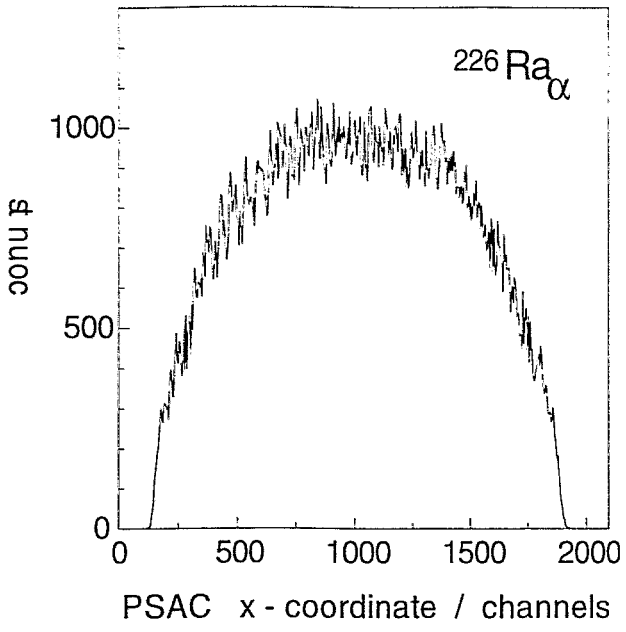

Fig. 6 Coordinate spectrum of a PSAC measured using a ^{226}Ra α-source.

A typical coordinate spectrum measured with a ^{226}Ra α-source is shown in fig. 6. The shape corresponds to the aperture defined by the PSAC against the point-like source. The image of the supporting structure of the window foil of the BIC can be seen in the coordinate scatterplot of fig. 7.

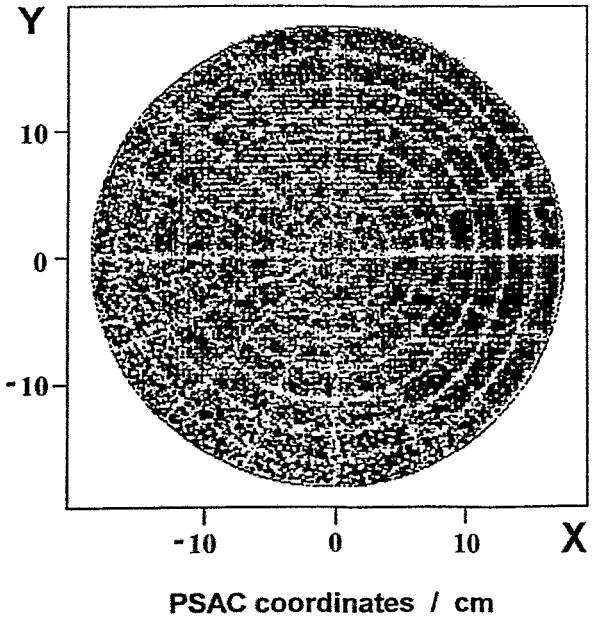

Fig. 7 Shadow zone in the coordinate scatterplot of a PSAC imaging the supporting structure of the window foil of the BIC. The plot is generated by correlated events in the PSAC and the BIC positioned behind it.

A rough selection of heavy fragments by their masses can be carried out using the ΔE versus TOF scatterplot of the PSAC (fig. 8). The E_R versus TOF scatterplot (fig. 9) delivers information about the ratio between correlated and random events, which is necessary for the correction of the results for a beam micro-structure unstable in time. In most cases a deflecting

high voltage near the target cannot be applied due to the residual pressure inside the central vacuum chamber mainly caused by the diffusion of the working gas of the BICs through the thin window foils. Therefore, a considerably high δ-electron background ($\approx 10^7 \div 10^8$ s^{-1}) correlated with the beam bunches has to be handled by the PSAC electronics.

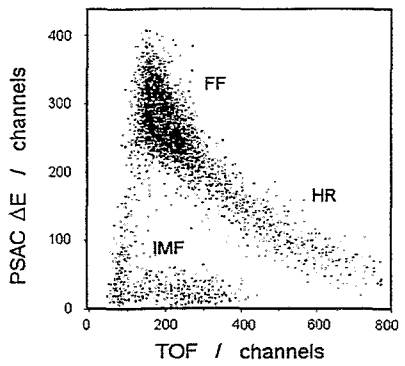

Fig. 8 ΔE versus TOF scatterplot measured by a PSAC for the reaction ^{14}N (53 AMeV) + ^{197}Au. (FF - fission fragments, HR - heavy residues, IMF - intermediate mass fragments)

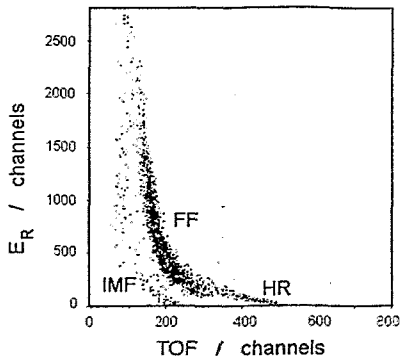

Fig. 9 E_R versus TOF scatterplot measured by a gas-detector module for the reaction ^{14}N (53 AMeV) + ^{197}Au. (Note that the time interval of the registration of heavy residues is considerably shorter than in the case shown in fig. 8.)

Two advantages of the detector concept of FOBOS should be emphasized :

(i) The long flight path and the timing properties of the PSAC make it possible to apply the TOF-E_R-method for the mass determination of the fragments instead of the ΔE-E-method which has its natural energy limits caused by the ΔE-detector. In other systems often heavy fragments (FFs, HRs) cannot be identified, e.g., at the 4π-array INDRA [12] where small ionization chambers deliver the ΔE-information, but timing cannot be used, or at the MSU 4π-array [9] where the compact detector design required more thick entrance windows of the BICs leading to considerably high registration thresholds.

(ii) The excellent spatial resolution of the PSACs together with the above mentioned principle of mass determination enables a more precise evaluation of the linear momenta of the fragments.

2.3 Axial ionization chambers

The principle of a BIC was first described in ref. [13]. Since the electric field is parallel to the direction of the incoming particles, the registered pulse-shape of a fragment stopped within the gas volume of the BIC represents an image of the specific energy loss along the ionization path characterized by the Bragg curve. The integral of the created electronic charge is proportional to the residual energy (E_R) of the fragment, and the maximum of the ionization-density distribution in the stopping path is a smooth function of Z (see also section 4.1.2).

A sketch of the lay-out of the detector module is shown in fig. 10.

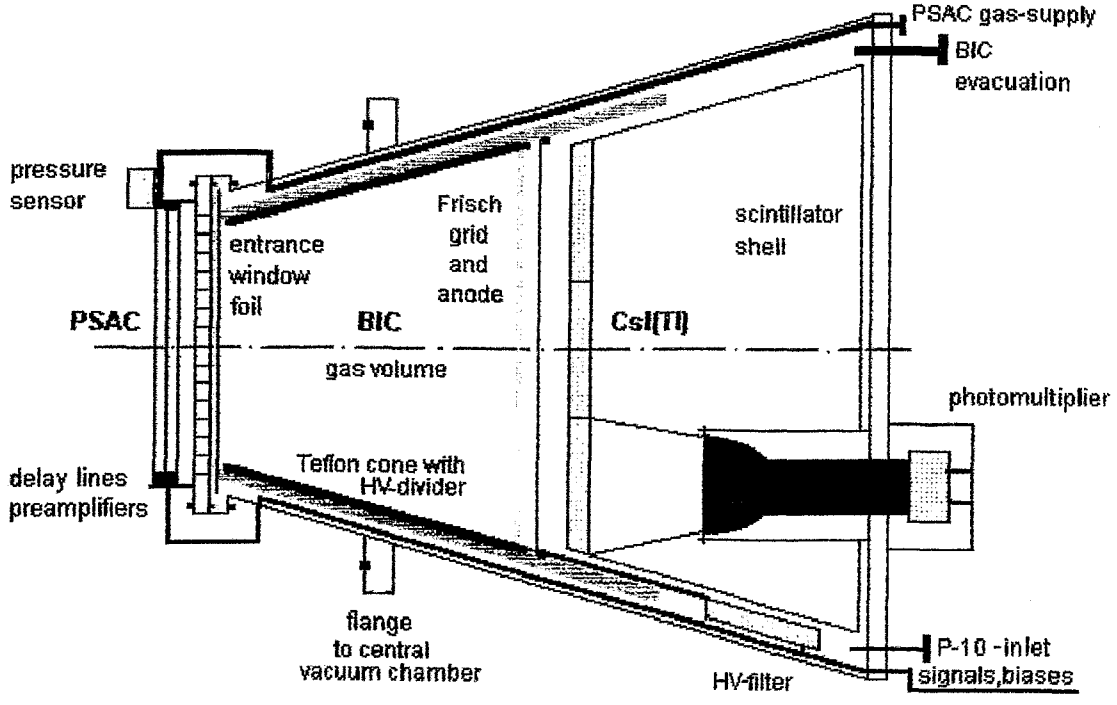

Fig. 10 Sketch of the general lay-out of a detector module.

The entrance windows of the large and small BICs, made of 1.5 ÷ 3 μm thick aluminized Mylar, have diameters Ø 385 mm and Ø 285 mm, respectively. The sensitive depth of the BICs is 250 mm. To withstand the pressure of the working gas, the delicate window foil, which at the same time serves as cathode, has to be supported by a twofold

structure — a concentric heavy carrier of a transparency of 94 % and an adjacent etched Ni-mesh having a cell dimension of ∅ 2.7 mm. Cells smaller than ∅ 3 mm are necessary because, otherwise, the extremely thin foils would not hold gas pressures up to 100 kPa needed to stop most of the IMFs within the sensitive depth. This mesh, however, reduces the transparency of the entrance window to 75 %, causing the most serious restriction with respect to the effective solid angle ($\Delta\Omega$) of the spectrometer.

The PSAC foils and the BIC window foil create together a dead layer for fragment spectroscopy of $\approx 0.7 \div 0.9$ mg cm^{-2}. The residual energy threshold for FFs (≈ 0.3 AMeV) is lower by a factor of ≈ 4 compared to the MSU 4π-array [9], while $\Delta\Omega$ is smaller by a factor of ≤ 2. For the registration of FFs, having typical c.m. energies of $0.5 \div 1.5$ AMeV, this seems to be a good compromise.

The shaping of the axial electric field is performed by 5 mm spaced Cu-strips coated on the inner side of the conical Teflon insulator. The voltage divider provides equal potential steps. The advantage of using a homogeneous field, also in a BIC with a large aperture, was already demonstrated in ref. [14].

The Frisch grid is placed 10 mm in front of the anode. It consists of two perpendicular wire-planes (50 μm thick Cu-Be spaced by 1 mm). The anode is a 10 μm thick aluminized Mylar foil. The positive voltage is fed to the anode and the Frisch grid via a passive filter and an attenuator to achieve optimum field strength relations [15]. In typical experiments the BICs are filled with a P-10 gas-mixture (90 % Ar + 10 % CH_4) at a pressure of $20 \div 40$ kPa and operated with an anode voltage of $1.5 \div 3$ kV. At the design limit of 100 kPa this voltage reaches 8 kV.

Conventionally, the charge signal of a BIC is split and shaped by two different time constants to deduce the E_R- and Z-information. In our case, the long electron drift-time (up to 4 μs) would cause a considerably large ballistic deficit. Therefore, a new processing method has been developed which derives the E_R- and BP-signals directly from digitized signal samples. The electronic set-up of this method has been published earlier [16], and its principle is shown in fig. 11. The read-out system consists of a charge-sensitive preamplifier, a Bragg curve digitizer (BCD) and a Bragg digital processor (BDP). The BIC-signal is shaped by a short time constant ($\tau = 0.2$ or 0.4 μs) in a spectroscopic amplifier and further digitized by an 8-bit flash ADC with a quartz-stabilized sampling frequency of 10 MHz. When a signal is recognized by the threshold comparator, two arithmetic units are activated calculating the

values for E_R and BP. The algorithms are schematically displayed in the bottom of fig. 11. The hatched areas indicate the sums over the samples. The control logics (not shown in fig. 11) organizes the coincidence condition with respect to the PSAC, a pile-up inspection, and the connection with the first-level trigger. The digital-processing system (two CAMAC modules per FOBOS module) is very simple to operate, faster than a conventional one by a factor of ≈ 10, and about two times cheaper. An energy resolution of the BIC of 89 keV was achieved for ^{238}Pu α-particles.

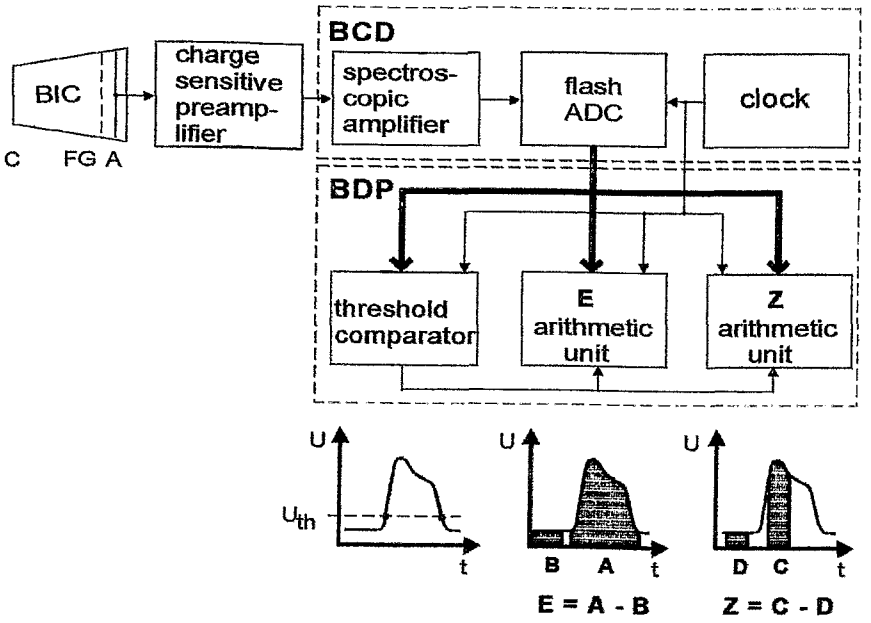

Fig. 11 Principle of the digital-processing method of the BIC signal. (C - cathode, FG A - Frisch grid and anode, BCD - Bragg-curve digitizer unit, BDP - Bragg digital-processor unit) The hatched areas A, B, C, D indicate the sums over the samples.

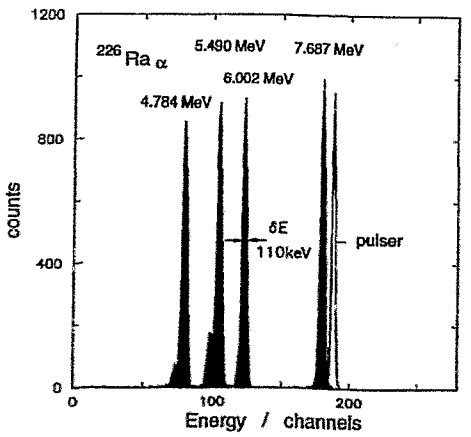

An energy spectrum measured with a ^{226}Ra α-source is shown in fig. 12.

Fig. 12 Energy spectrum of a ^{226}Ra α - source measured by a BIC. The energy resolution at 6 MeV amounts to 1.8 %.

A BP versus E_R scatterplot measured for the reaction ^{14}N (34 AMeV) + ^{197}Au [17] is shown in fig. 13. The charge resolution obtained around Al is $Z / \Delta Z = 65$. Elements are resolved from He up to about Fe.

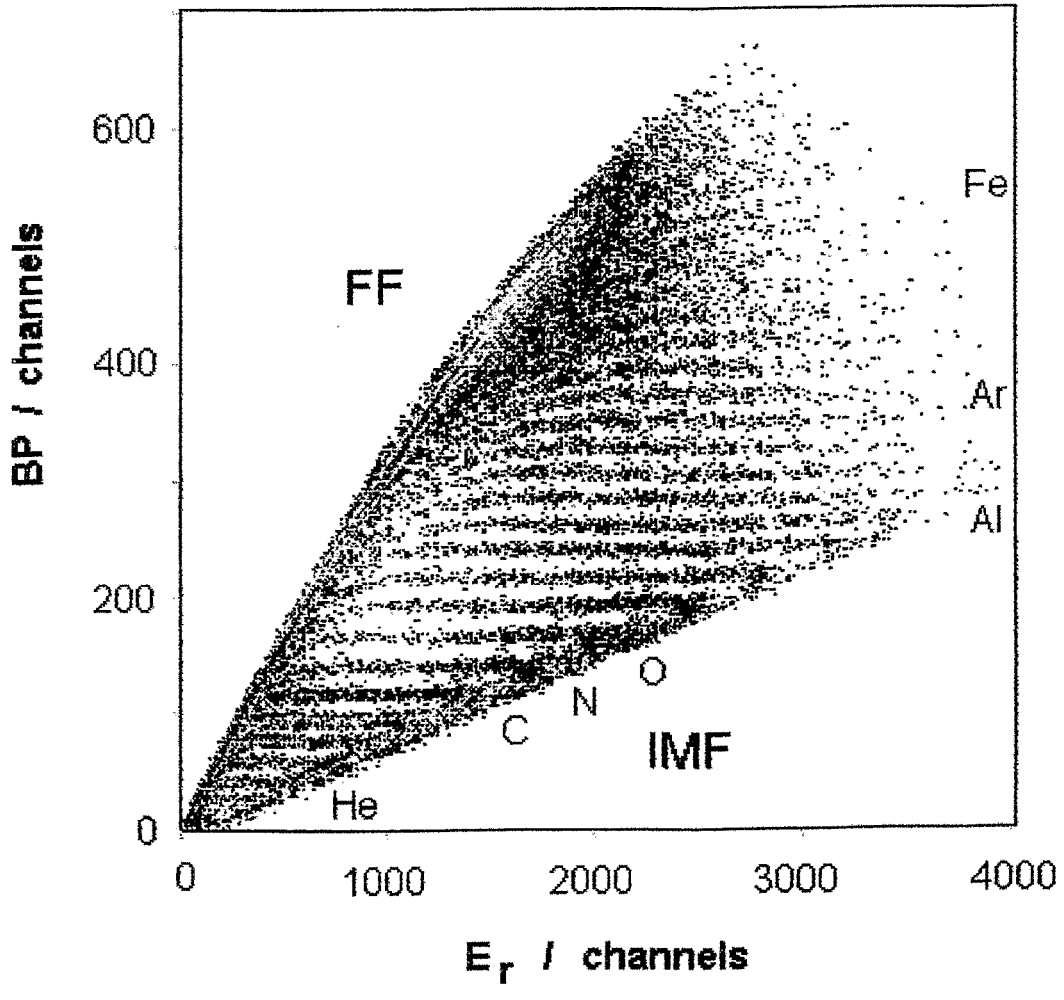

Fig. 13 Bragg peak-height (BP) versus residual energy (E_R) scatterplot of inclusive fragments measured by a BIC for the reaction ^{14}N (34 AMeV) + ^{197}Au. Particle branches of several resolved elements are indicated. (FF - fission fragments; IMF - intermediate mass fragments)

2.4 Evacuation and gas - supply system

The central vacuum chamber is evacuated by three turbomolecular and four cryogenic pumps achieving an effective pumping speed of 5000 l s^{-1}. The critical leakage is caused by the pressure-dependent diffusion rate of the chamber gas through the window foils of the BIC. To avoid additional leakage caused by mechanical defects, the supporting Ni-meshes had to be tooled very carefully, and all the foils were checked for leakage at a separate test-stand before they were mounted on the BIC. At a total foil leakage rate of ≈ 0.2 mbar l s^{-1}, which is about twice the theoretically expected diffusion rate at typical BIC pressures, an ultimate vacuum of $\approx 10^{-4}$ mbar can be reached inside the central vacuum chamber.

The gas-filled detectors of FOBOS are operated in a flow-through regime to guarantee stable long-time working conditions. To prevent damage of the thin window foils, all manipulations, i.e. the evacuation from atmosphere, gas-loading, gas-flow and gas-pressure stabilization, gas-evacuation, air-inlet etc., have to be carried out in a strict order and with sufficiently long time constants. At every time, a full knowledge of the status of the whole apparatus is necessary. Therefore, a computer-controlled evacuation and gas-supply system was developed [18, 19].

The gas-detector modules are divided into 10 independently operated groups of three modules each. The inputs and outputs of the PSACs and BICs are connected via individual valves and flexible pipes to the collector rings, located at the front and rear sides of FOBOS (fig. 2), and further to the mass-flow regulators of the gas-inlet and the pressure stabilizers and evacuation system, respectively.

Special sensors and mini-valves are mounted directly to the PSAC frames to limit the pressure gradients at the PSACs to a value of ≈ 1500 Pa. In the case of accidental pressure mismatching the mini-valves immediately connect the PSAC volumes with the central volume. The total leakage rate through the PSAC window foils is about one order of magnitude lower than that through the BIC window foils.

The P-10 gas for the BICs is mixed on-line by controlling the respective mass-flows of the components. A gas analyzer is permanently checking the gas composition as necessary test for fixing the electron drift-time, and with it the energy resolution of the BICs during a long-time experiment. Several series of tests were performed to optimize the gas flow-through regime. For example, the influence of the gas quality on the signal amplitude of a BIC [20] is shown in fig. 14. The gas exchange rate of the BICs can be adjusted at the inlet collectors. A full gas exchange takes about 6 hours. All pressures are stabilized to an accuracy of 1 %.

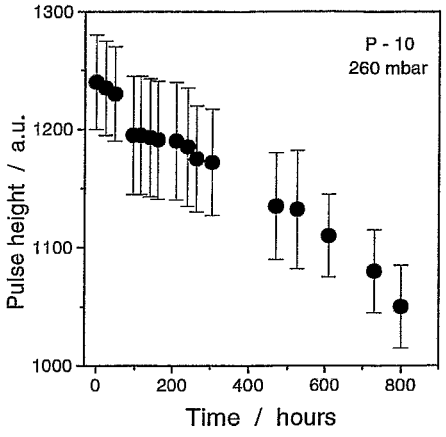

Fig. 14 Influence of the changing gas quality on the signal pulse-height of a BIC operated in a stationary regime with P-10 at a pressure of 260 mbar.

The computer control of the evacuation and gas-supply system of FOBOS is based on a Siemens SX Automation System including graphical visualization of the status on an X-terminal (fig. 15).

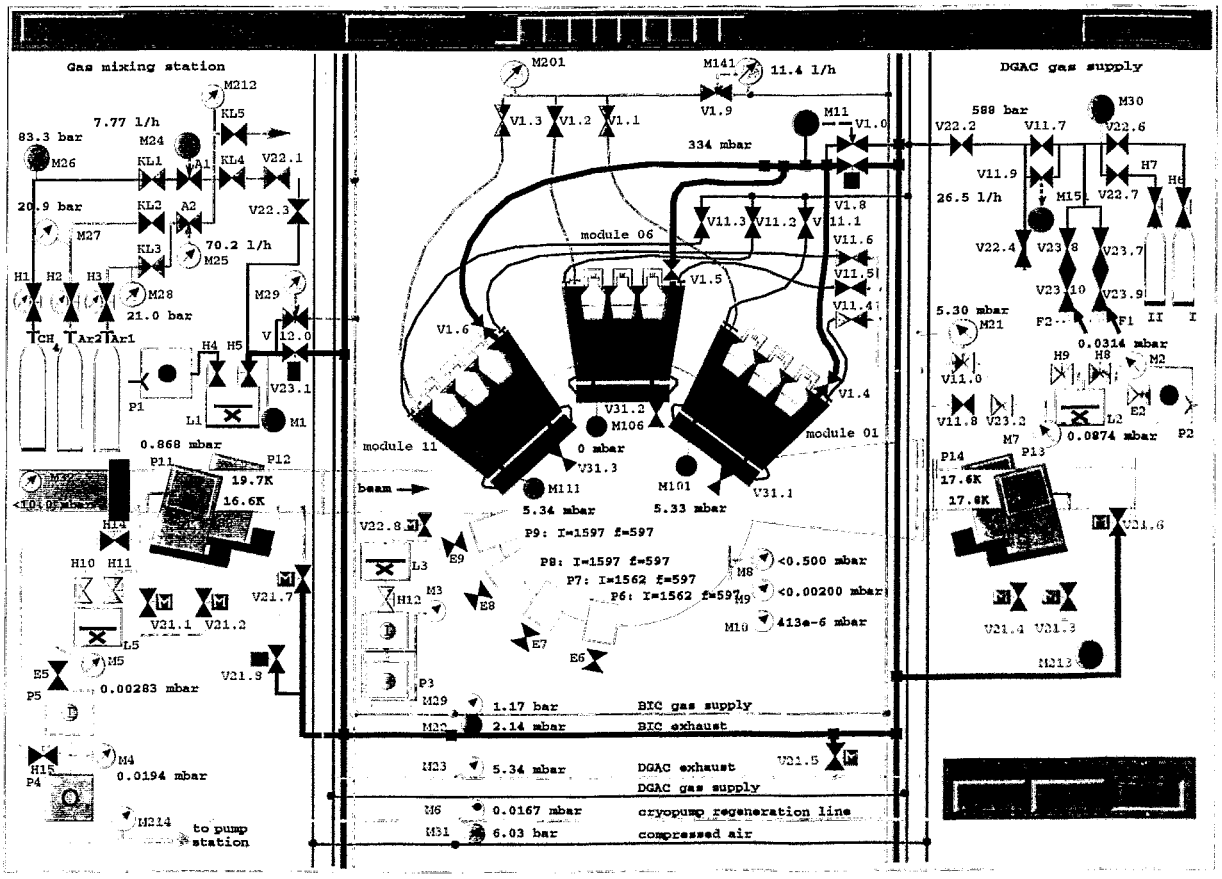

Fig. 15 Graphical visualization of the status of the evacuation and gas-supply system on an X-terminal. The remote control of some evacuation devices is possible.

The instant pressure values at 63 measuring points and the gas flows through 11 regulators are recorded on-line by a SUN Sparcstation SLC and visualized for inspection. During the operation a full protocol of the entire system is created (fig. 16).

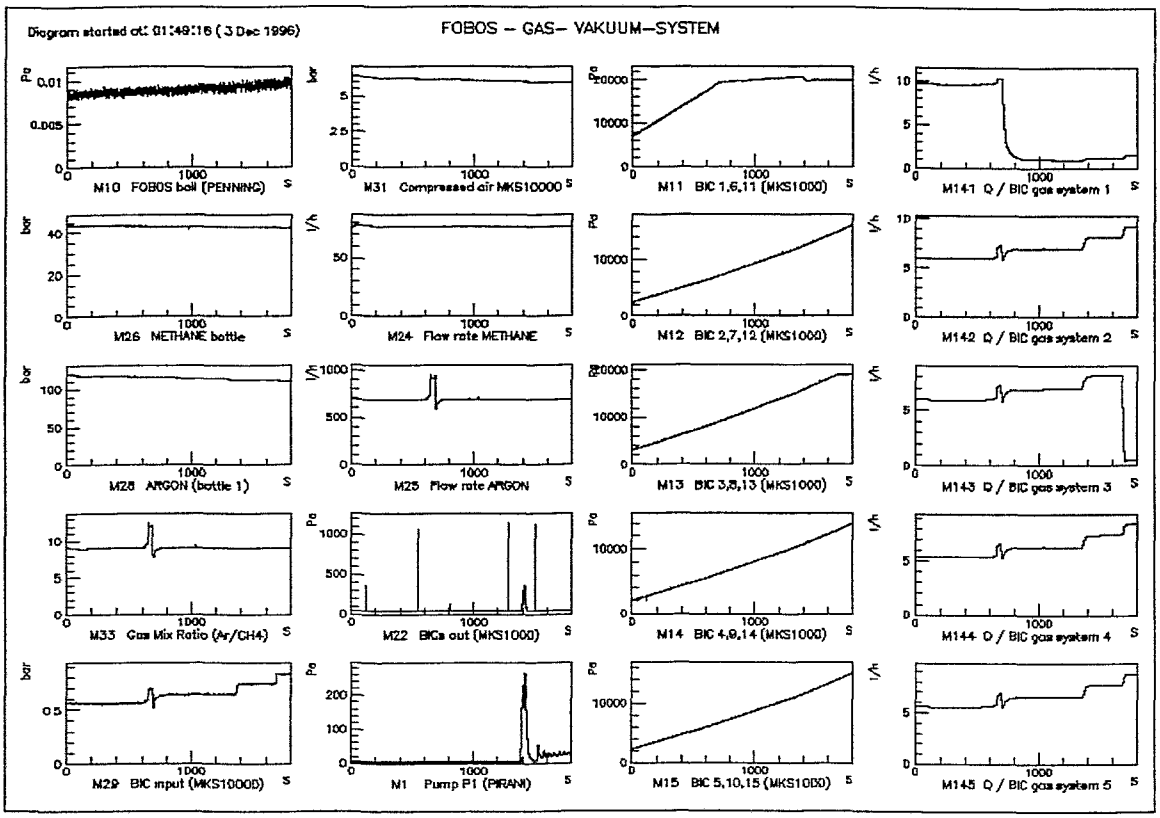

Fig. 16 Snapshot of the on-line protocol of the operation of the evacuation and gas-supply system generated on the SUN SparcSLC terminal.

As an example, the process of the controlled gas inlet into five of the BIC (M11 - 15, third column) is shown. The immediate reactions of the vacuum in the central chamber (M10), of the P-10 gas pressure at the BIC input (M28), of the methane and argon flow rates (M24, M25), the stability of the on-line gas mixing ratio (M33), and the pumping speeds at the BIC outputs (M142 - 145) are followed in time to avoid any damage in the gas-detectors.

2.5 Scintillator shell

A shell of CsI(Tl) detectors [7,8] is arranged behind the BICs to register low ionizing LCPs and energetic IMFs which penetrate the gas-filled detectors. It consists of 210 hexagonal-shaped crystals of thicknesses 15 mm and 10 mm at angles of $\vartheta \approx 19^\circ \div 52^\circ$ and $\vartheta \approx 53^\circ \div 162^\circ$, respectively. These thicknesses make it possible to stop protons and α-particles with energies up to 64 AMeV and 50 AMeV, respectively. The angular resolution is limited by the dimensions of the crystals to $10^\circ \div 12^\circ$.

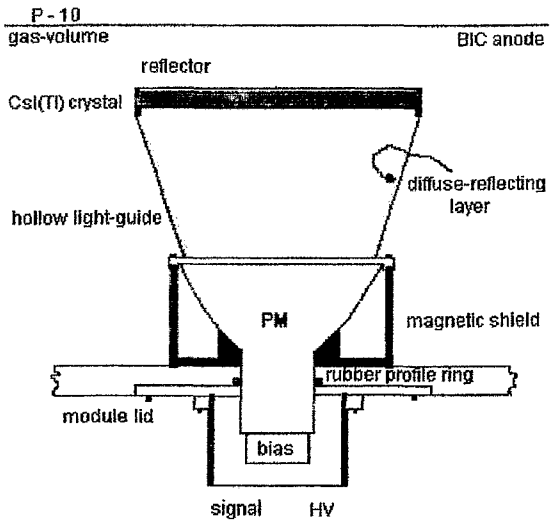

The scintillators are coupled by hollow diffuse-reflecting light-guides to large-area spectroscopic photomultipliers of the types FEU 167 (Ø 120 mm) and FEU 173 (Ø 170 mm) (fig. 17). A 2 μm thick aluminized Mylar reflector in front of the crystals enhances the light output.

Fig. 17 Sketch of the general lay-out of a CsI(Tl) scintillation detector (PM -photomultiplier).

The detectors are optimized to have a weak position dependence of the light collection (≈ 5 %) and a typical energy resolution of ≈ 8 % for α-particles at 5 MeV energy [7]. The photomultipliers are surrounded by cylindrical magnetic shields.

The LCP-identification is carried out by application of the pulse-shape analysis method [22]. Governed by the intrinsic features of Tl-activated CsI the pulse-shape of the scintillation light depends on the ionization density in the particle track. The pulse-shape is characterized by several components of different decay times. The decay time of the fast component (τ_{FAST}) and the ratio of amplitudes of the main slow to the fast component (h_{SLOW} / h_{FAST}) are smoothly decreasing functions of the stopping power (dE / dx) [23]. Integrating the current signals of the photomultipliers within two well-adjusted timing gates (FAST : $\Delta t_1 = 0 \div 400$ ns; SLOW : $\Delta t_2 = 1600 \div 3600$ ns) LCPs with $Z \leq 3$ are well

separated by their atomic and mass numbers. A scatterplot illustrating the LCP-identification is given in fig. 18.

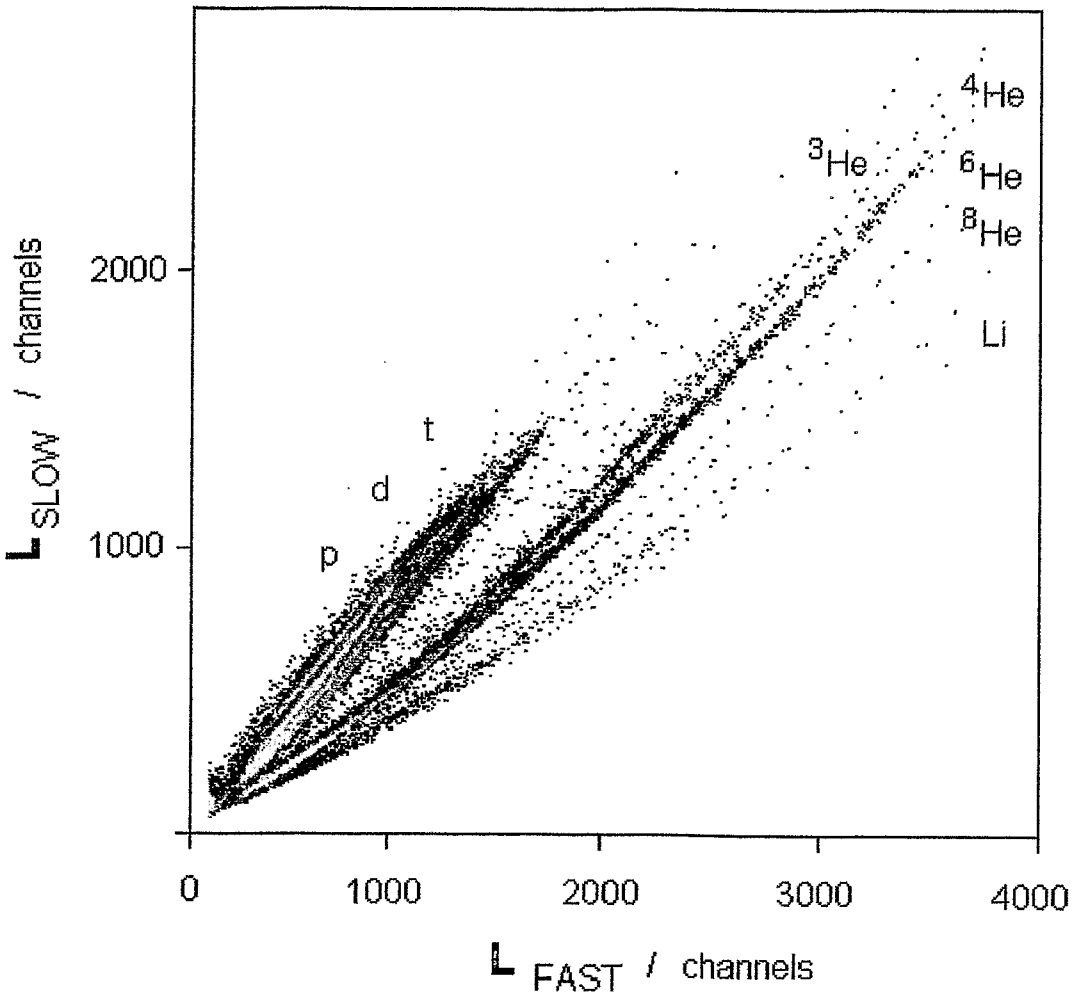

Fig. 18 Scatterplot of the LCP-identification matrix (L_{SLOW} versus L_{FAST}) measured by a CsI(Tl) scintillation detector applying the pulse-shape analysis method. The particle branches of protons, deuterons, tritons, He-isotopes and Li-isotopes are indicated.

Correlated events in a PSAC and a scintillation counter image the geometry of the CsI(Tl) crystal (fig. 19). The particle identification of such events (e.g. energetic IMFs penetrating the BICs) can also be performed by the ΔE-E-method (fig. 20) using the energy loss in the BIC (ΔE_{BIC}) and the light output (E_S) of the scintillator. By this means the

dynamical range of the FOBOS detector is considerably enlarged with respect to IMF spectrometry.

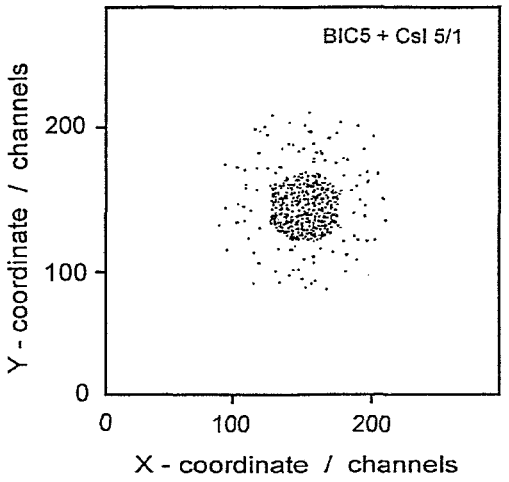

Fig. 19 Coordinates scatterplot of correlated events recorded by a PSAC and a CsI(Tl) detector positioned behind it. The geometry of the CsI(Tl) crystal is imaged.

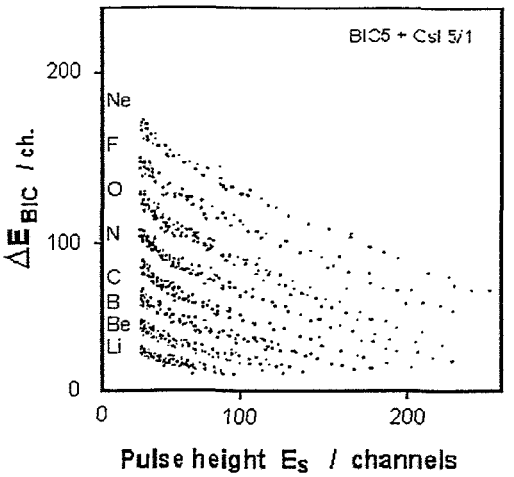

Fig. 20 Charged - particle identification matrix measured by application of the ΔE-E-method. (ΔE_{BIC} - energy loss in the BIC; E_S - residual pulse - height of the fast part (L_{FAST}) of the CsI(Tl) detector signal)

2.6 Forward array

For geometrical reasons the minimum acceptance angle of the FOBOS spectrometer is $\vartheta \approx 21°$. Forward directed fast reaction products cannot be registered by the gas detectors. Therefore, part of the former ARGUS detector array [24] was modified to be used as a forward array at FOBOS. It can be installed inside the central vacuum chamber through the forward (exit) cone (fig. 2). The detector geometry of the forward array is given in tab. 2. The forward array consists of six concentric rings of altogether 92 phoswich detectors, each being a combination of a 0.5 mm thick fast scintillator (Pilot-U) and a 20 mm thick slow BGO scintillator. This allows one to stop protons (α-particles) with energies up to $\approx$ 100 AMeV. The element identification is possible up to $Z \approx 15$ with a threshold for LCPs of $\approx$ 5 AMeV.

A simple pulse-processing concept [25] has been modified for its application to phoswich detectors. The idea was to separate the fast component (L_{FAST}) of the phoswich light

pulse (L_{TOTAL}) by a specific analog differentiation of the current signal of the photomultiplier. Only two integration gates (Δt_{FAST} = 100 ns and Δt_{TOTAL} = 400 ns) common for all phoswich detectors are then necessary.

A particle-identification matrix (L_{FAST} versus L_{TOTAL}) of a phoswich detector measured for the reaction ^{40}Ar (36 AMeV) + ^{248}Cm is given in fig. 21. Fast projectile-like fragments of all possible Z can be observed, and also particle branches of H- and He-nuclei and light IMFs. Since the element resolution of a phoswich detector strongly depends on the exact setting of the integration gate of the fast component, a slightly lower resolution compared to the case of using individual integration gates for all the detectors [24] is expected. Nevertheless, this read-out system is very compact and not expensive.

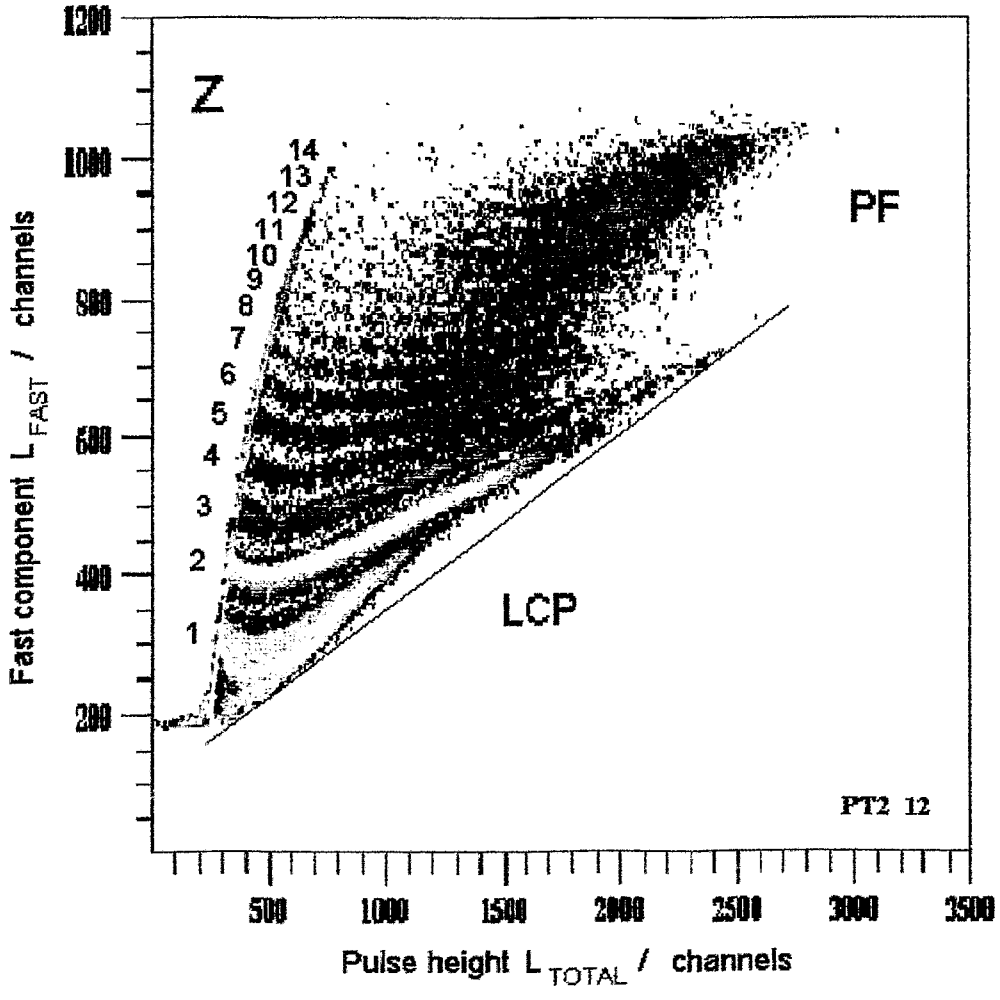

Fig. 21 Charged - particle identification matrix (L_{FAST} versus L_{TOTAL}) measured by a phoswich detector of the forward array at $\vartheta = 8^{\circ}$ for the reaction ^{40}Ar (36 AMeV) + ^{248}Cm (PF - projectile-like fragments, Z - atomic number of charged particles identified).

3. DATA ACQUISITION SYSTEM

3.1 First - level trigger

The first-level trigger of FOBOS [21] is usually generated by the gas detector part, while the scintillators are read-out in the slave mode. In special cases a trigger can also be set by the scintillator shell and/or the forward array. The entire TTL/ECL-based hardware of the trigger logics fills one CAMAC crate. It delivers either the LAM demand for data storage or a general RESET if after an inspection the event pattern requires a rejection of the event.

Provided the digital processor (BDP) is not busy, a timing signal of the corresponding PSAC passes a special blocking and pile-up inspection unit (LBIN) which is connected with the control logics of the BDP. Then, an event gate is opened for a duration of $\Delta t = 200$ ns, a bit in the coincidence pattern register is set, and a TDC is started, which will be stopped by the next arriving RF-signal from the cyclotron. The event pattern is analyzed by a majority coincidence unit connected with the central event selector which induces a LAM demand if a preset multiplicity condition is fulfilled and there was no signal pile-up. Optionally, the following conditions may be used either to reject the event or to label the affected parameters :

(i) There is another PSAC signal in the time intervals 12 μs before and 6 μs after the event, respectively.

(ii) There was another BDB threshold-comparator response in the time interval 10 μs before the event.

(iii) The trailing edge at the threshold-comparator of the BDP is outside a certain time interval related to the maximum electron drift-time of the BICs.

After a LAM demand has been recognized, the VME processor first reads the coincidence pattern register and then the conversion results of the TDCs (TOF) and BDPs (BP, E_R) which had fired. Subsequently, the QDCs of the scintillator shell and the forward array are serviced. Consequently, the blocking signals (BLK) of the LBINs are removed, and the system is ready for handling the next event.

The counting rates for events of different fragment multiplicity naturally differ by orders of magnitude. A special unit (major divider) which allows one to modify the accepted rates concerning the event multiplicity was developed to optimize the data storage.

A principal scheme of the front-end electronics of a gas-detector module and part of the first-level trigger is shown in fig. 22.

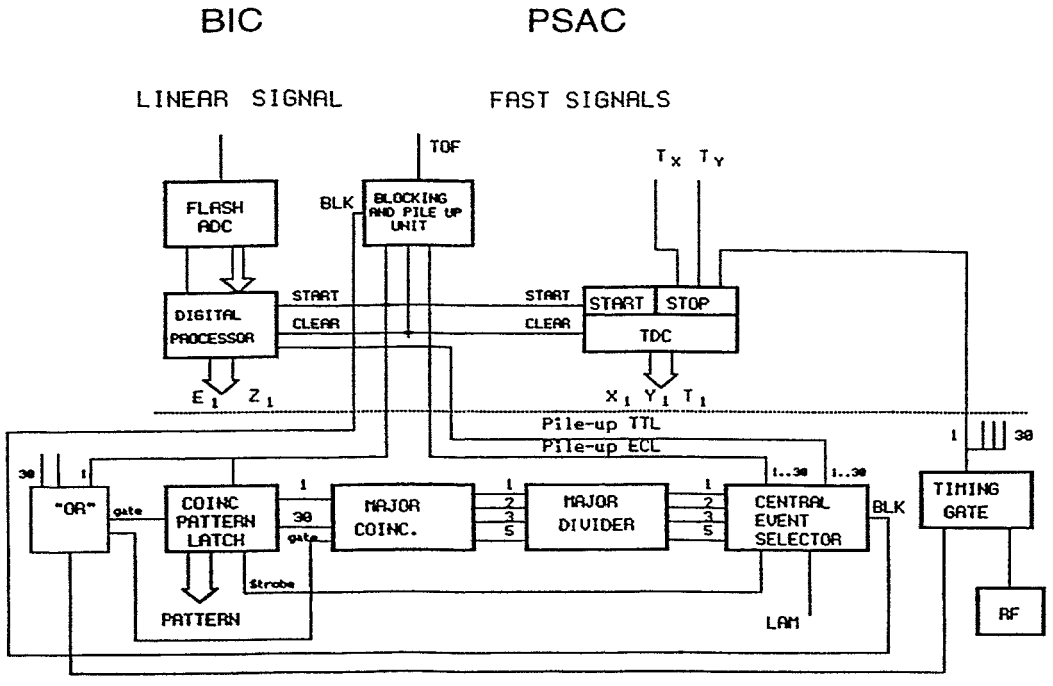

Fig. 22 Front - end electronics of a gas - detector module and part of the first - level trigger. (LAM - "look-at-me" CAMAC signal; BLK - blocking signal; RF - radiofrequency signal from the cyclotron)

3.2 Read - out electronics

Ten CAMAC crates housing the digitizing electronics of the gas-detector part and the control logics, and one FASTBUS mini-crate used for the photomultiplier read-out of the scintillator shell and the forward array, are connected with a main VME crate by means of the parallel VSB Differential Bus Extension (VDB bus). The VDB bus is well suited for multi-crate systems where different bus standards have to be controlled. A single-board computer EUROCOM-6 with a 68030 CPU builds the event data blocks [26].

The CAMAC-to-VSB interface is a single-width CAMAC crate controller STR 610 / CBV [27] driven from the VME Subsystem Bus (VSB) via the VSB Differential Cable. The specification of the CBV is similar to the CAMAC crate controller of type A1. It maps a portion of the VSB address space to the CAMAC - "C,N,A,F" and generates single CAMAC cycles from each proper VSB cycle.

The FASTBUS mini-crate contains a 68030-processor board (CERN Host Interface, CHI), an I/O-Port, a LAN Ethernet module [27] and six 96-channel FASTBUS QDCs

(C.A.E.N. F683C [28] and LeCroy [29]). The VSB I/O-Port provides an efficient interface between the CHI and the VME workstation where the CHI is operating in the VDB slave-mode. The CHI data memory is directly mapped into the local VSB address space, and the EUROCOM-6 processor module is treated in the same manner as any local memory.

The VME workstation sends the data blocks via Ethernet (LAN) and a fiberoptical link to a SUN Sparcstation-10 which writes them "event by event" to the mass storage memory. The architecture of the data acquisition system is schematically shown in fig. 23. The maximum data rate with respect to the gas-detector part of FOBOS is about 200 kbyte s^{-1}. Due to the conversion time of the FASTBUS QDCs (1 ms) residual rates of 50 ÷ 100 kbyte s^{-1} are typical for the whole spectrometer. Therefore, the maximum permitted counting rate of FOBOS becomes ≈ 500 ÷ 1000 events s^{-1}. This rate is, however, restricted by other experimental requirements, e.g., a low rate of random coincidences etc.

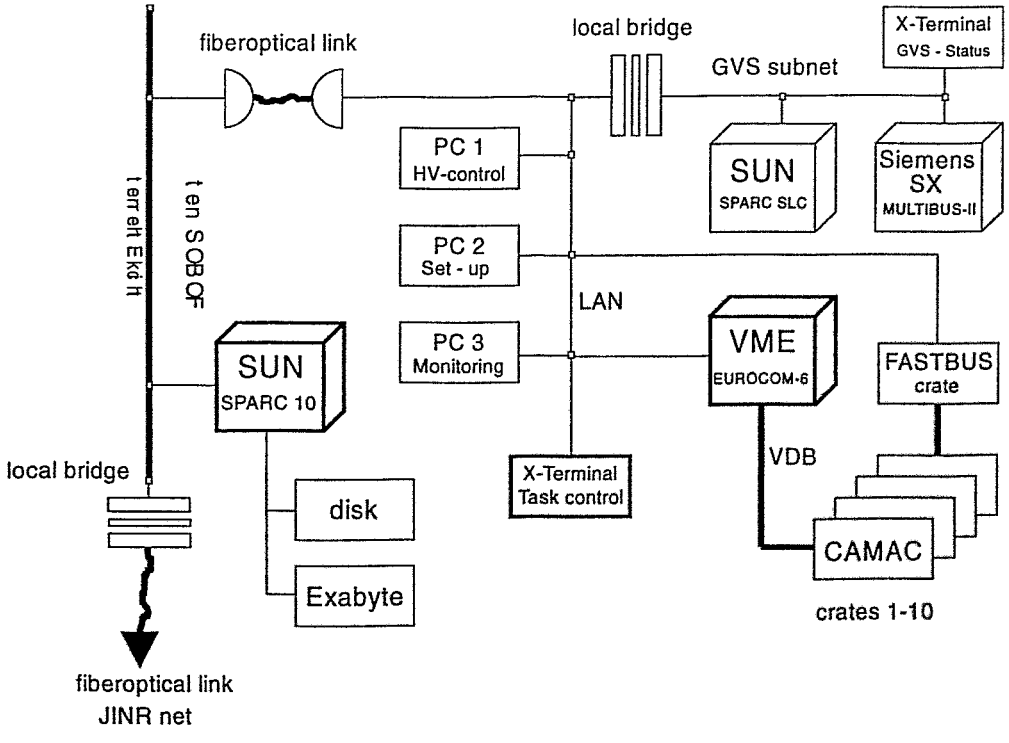

Fig. 23 Architecture of the data acquisition and the gas-vacuum system (GVS) network. (LAN - local net; VDB - VSB differential bus)

The EUROCOM-6 and the CHI are operating under the Microware real-time operating system OS-9 (professional). All time-critical tasks are moved to the module processors. The data acquisition control program (COLLECT) runs on the SUN Sparc-station -10. Quasi-on-line monitoring of the recorded data is performed using several AT 486 personal computers (PC) and the ATHENE data analysis software [30] which via LAN organizes a direct access to the data just written to the disk memory of the SUN Sparcstation -10.

3.3 Experimental data structure

The list-mode data structure is adopted from the VMS-based data acquisition system HOOPSY [31] in order to use the available OLYMP data analysis package [32]. It is module-oriented by an event-pattern register containing information about fired PSACs, CsI(Tl) detectors and groups of phoswich detectors. Up to 10 parameters can be defined to be read out in correlation with one pattern bit, and altogether 2000 parameters can be handled by the program COLLECT. On average, a valid event is characterized by about $30 \div 40$ parameters which are stored within less than 2 ms.

The data file structure is characterized by sequential event storage into data blocks of fixed length. A header containing information about the data file structure (defined parameters) is assigned to the ATHENE program for quasi-on-line or off-line data analysis.

3.4 Data analysis software

The ATHENE code [30] was especially designed for a distributed analysis of the data obtained at the FOBOS spectrometer using IBM PCs of type AT 386/486. A new more powerful version (ATHENE94) [33] written in the object-oriented language C++ [34, 35] was developed for real-time data processing on computers with UNIX-like operational systems and an X-WINDOWS environment [36].

The program allows to read data written in the formats of the programs CAMDA [37], HOOPSY [31] and OLYMP [32]. Special transformation algorithms to read data written in other formats are available.

Via the menu, the user has the possibility to accumulate and to visualize up to 20 ordinary histograms and up to 50 color scatterplots, he can produce new data files reduced in the event dimension and/or selected by sorting conditions (gates) in the formats of CAMDA or OLYMP. The user can also execute a number of analysis operations acting on these histograms, such as simultaneous displaying of several histograms, linear/logarithmic scaling,

setting gates within the histograms or scatterplots, calculating spectrum parameters and statistics, etc. He can interactively drive the process of data accumulation by setting both the parameters and relevant selection criteria for every histogram, scatterplot or output data file. All the configuration conditions concerning parameters, histograms, plots, gates, selection criteria, etc. as well as the content of any histogram or plot can be saved to a disk file and retrieved.

4. CALIBRATION PROCEDURES

4.1 Calibration of the parameters measured by the gas - filled detector modules

The use of gas-filled detectors for the measurement of charged particles implies the important advantage, that there is a linear and charge-independent correlation between the stored raw data and the corresponding physical values. Hence, the transformation of the measured data — the PSAC-coordinates (X,Y), the fragment TOF and energy E_R — into physical units requires the determination of only two calibration constants for each of the parameters.

However, in any case it is necessary to record some calibration events within the collected spectra, which result from fragments with known quantities. A well established practice to generate such events is to carry out special measurements with calibration sources (e.g. α-particle emitters or spontaneously fissioning nuclides) or the impinging of elastically scattered beams. Unfortunately, this method involves some general difficulties. The first of them is caused by the energy loss of any fragment within the target layer. Furthermore, the general requirement of identical conditions for the calibration and the data taking measurements fails.

An alternative method applied in the present work delivers an intrinsic calibration based on the original raw data only. In the following the measured parameters (in channel units of the ADC devices) are denoted for convenience in capital letters, the calibrated physical values (in units of cm, ns, MeV etc.) in small letters.

4.1.1 Calibration of the coordinates of the position-sensitive avalanche counters

The absolute coordinate calibration of the PSACs is performed by using coordinate scatterplots of events measured in coincidence with the BICs positioned behind them. The supporting structure of the window foil of the BIC generates a shadowed zone with a

decreased rate (fig. 7). A geometrical model of the supporting structure is adjusted to the center and to the dimensions of this image to achieve a complete agreement with the shadowed zone. This procedure gives the intrinsic scales which are used to define the module-oriented coordinates (x,y) of the registered event. The polar and azimuthal angles (ϑ,φ) of the particle with respect to the target position can be calculated in a straightforward manner with reference to tab. 1. The uncertainties (Δx, Δy) lead to errors of $\Delta\vartheta = \Delta\varphi \approx 0.2^{\circ}$.

4.1.2 Energy calibration of the Bragg chambers

The calibration procedure for the residual energy (E_R) of the fragments in the BICs makes use of the additional information concerning the fragment charge (Z), which is in particular available for IMFs from the Bragg-peak spectroscopy. This method of charge determination requires that the maximum of the energy-loss distribution (Bragg curve) of the fragment considered is located inside the sensitive volume of the BIC, i.e. between the cathode and the Frisch grid. In this case the measured Bragg peak-height (BP) is independent on the entrance energy of the fragment.

An analytic expression of the dependence of the BP on Z for particles stopped in a P-10 gas-mixture has been derived in ref. [38],

$$BP(Z) = C \cdot \exp\left(-18.95 \cdot Z^{-0.0721}\right) \qquad (1)$$

where C denotes a scaling factor which has to be determined experimentally. In a wide range the function BP(Z) can be rather well approximated by a linear expression (fig. 24). This leads to the nearly equidistant particle branches observed in fig. 13.

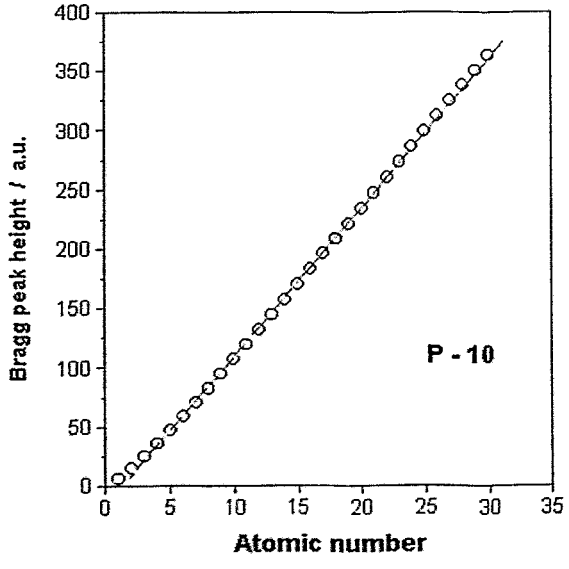

Fig. 24 Dependence of the Bragg peak-height (BP) on the atomic number (Z) of charged fragments stopped in a P-10 gas-mixture. The calculated values (eq. 1) are indicated by open circles. The line results from a linear regression analysis. It is defined by the expression

$$BP(Z)_{lin} = C^{*} \cdot (12.511 \cdot Z - 15.518).$$

In practice the measurement of the Bragg-peak requires a sufficiently large entrance energy, especially for heavier fragments. The lower energy threshold depends on the operation parameters of the BIC and the pulse-processing method, i.e. the electron drift velocity, the gas pressure, the integration time constant of the current pulse, and the total time interval of energy-loss integration. At typical operation conditions, the minimal necessary energy loss of an IMF for Z-identification amounts to $e_R^{min} \approx 0.6$ AMeV.

If the fragments are stopped in the gas volume of a BIC, the measured value E_R reflects the residual fragment energy at the *entrance* into the chamber gas (if the nuclear stopping is neglected or corrected for).

The situation changes for such kinetic energies which allow the fragments to pass through the entire chamber depth. In this case the energy loss within the gas-volume decreases with increasing entrance energy. This results is an upper limit for direct residual-energy measurement (e_R^{max}) and charge identification. It strongly depends on the composition and the pressure of the chamber gas, on the path length within the BIC, and on (A,Z) of the fragments. The upper energy thresholds e_R^{max} of the BIC were calculated for particles of $Z = 2 \div 10$ ($A = 2 \cdot Z \pm 1$) at P-10 pressures of 19, 32 and 45 kPa (fig. 25) by use of the range-energy code STOPOW [39]. The dependence of the specific energy loss on A was approximated by the range parametrization $R / A = r(E,Z)$.

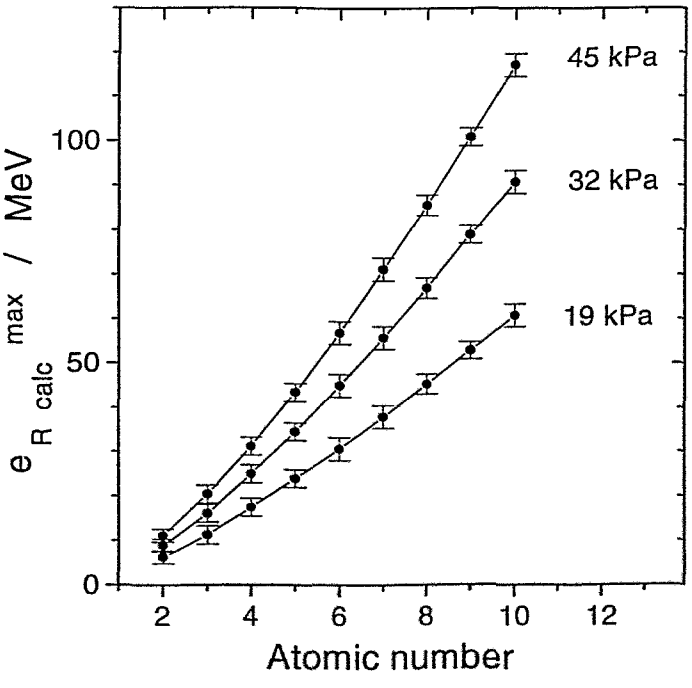

Fig. 25 Maximum energy losses in the gas volume of the BIC ($e_{R\ calc}^{max}$) calculated for selected particles at pressures of the P-10 gas-mixture of 19, 32 and 45 kPa.

Under the condition of sufficient statistics, the energy points E_R^{min} and E_R^{max} can easily be fixed for resolved Z-branches in the raw-data matrix BP versus E_R (fig. 13).

However, in particular for small Z, particle branches of different isotopes may overlap (fig. 26). This complicates the unambiguous fixing of E_R^{max}.

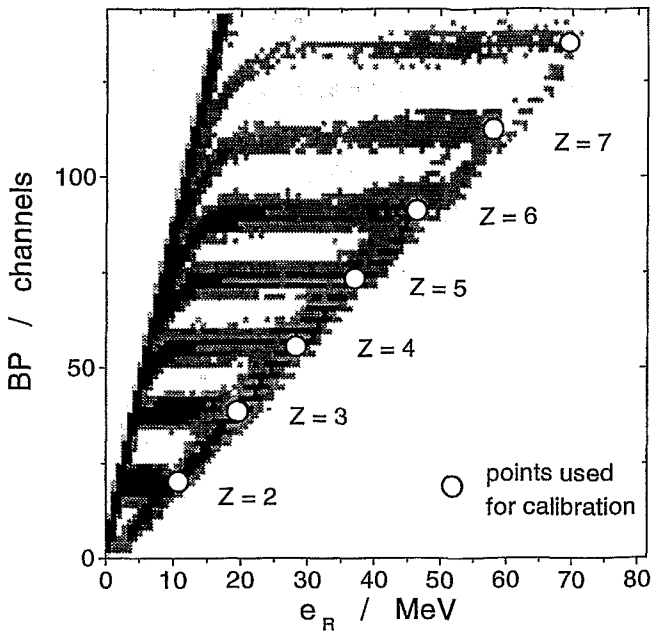

Fig. 26 Part of a Bragg peak-height (BP) versus E_R scatterplot of a BIC (cf. fig. 13). The events have been stored with respect to the calibrated energy scale (e_R). The points used for the calibration procedure are marked.

In addition to these calibration points, the BDB [16] guarantees that the value $E_R = 0$ corresponds with the ADC channel number "zero". The remaining slope constant for the energy-calibration curve e_R (E_R) is deduced by a linear regression analysis (fig. 27).

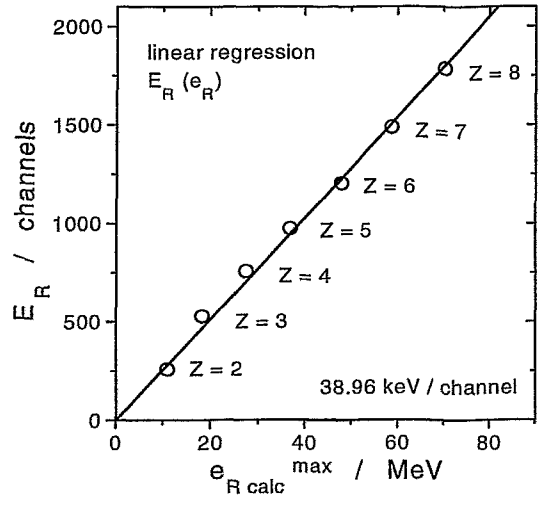

Fig. 27 Energy-scale calibration of the BIC comparing the calculated maximum energy losses ($e_{R\,calc}^{max}$) with corresponding values E_R measured for particles of $Z = 2 \div 8$. A linear regression analysis (line) delivers the slope constant of the calibration curve.

In order to perform a relative scaling between the BP-spectra of different BICs, the identified Z-branches are used for the determination of an "experimental" function $BP(Z)^{exp}$. (Note that this intrinsic calibration does not relate to eq. (1) !). A BP-spectrum of events

selected by gates over the energy intervals $E_R^{min} < E_R < E_R^{max}$ for each Z, respectively, is shown in fig. 28.

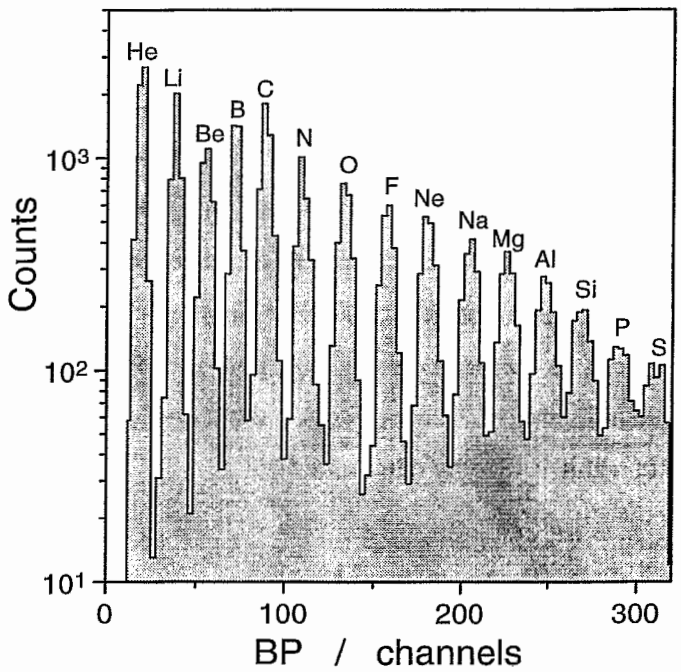

Fig. 28 Bragg peak-height (BP) spectrum of selected fragments at kinetic energies corresponding to the maximum specific energy losses.

The mean values <BP> of the peaks are compared with the corresponding Z in fig. 29. A linear regression analysis delivers the function $BP(Z)^{exp}$ which can be used for scaling purposes.

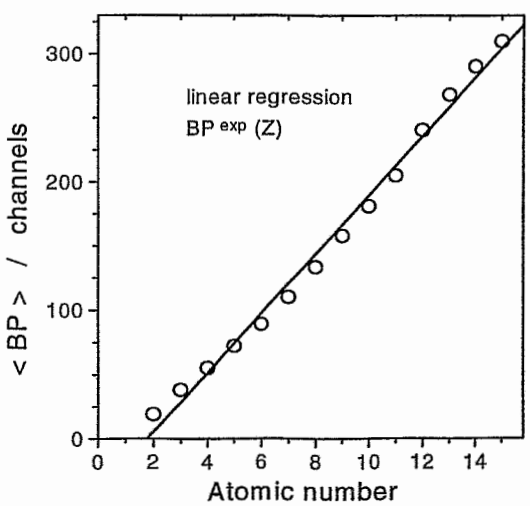

Fig. 29 Correlation between the mean measured Bragg peak-height (BP) values of the fragments and the corresponding atomic numbers (Z) for the same events as in the BP-spectrum shown in fig. 28. A linear regression analysis delivers the "experimental" scaling function $BP^{exp}(Z)$.

4.1.3 Time calibration of the position-sensitive avalanche counters

The absolute TOF calibration necessary for the determination of the fragment velocities is based on data selection according to Z, calibrated e_R and (ϑ,φ). The mass number (A) for a given Z was estimated with respect to the line of β-stability. Together with the calibrated coordinates (x,y), the geometrical set-up defines the individual TOF path-length d(x,y) of the fragments from the target to the PSAC considered. Taking into account all the parameters known up to this moment, the energy losses $\Delta e_i (Z, A, e_R, n_i)$ in the k detector foils of areal density n_i are successively calculated, starting from the entrance window of the BIC and following "backward" to the entrance foil of the PSAC. For simplicity it is assumed in the following that the fragment velocity is *constant* on the TOF path-length (d), but this procedure is also applicable in the general case, i.e. accounting for some energy loss *on* d (e.g. in the PSAC window foil). The tof-value is thereby determined by

$$tof^2 = A \cdot d(x,y)^2 \; / \; 2 \left[e_R + \sum_{i=1,k} \Delta e_i (Z, A, e_R, n_i(x,y)) \right] \qquad (2)$$

and can be compared with the TOF determined "event by event". The correlation between tof and TOF (eq. (3)) is shown in fig. 30.

$$tof = (TOF - TOF_o) \cdot \delta tof / \delta TOF \qquad (3)$$

The slope constant $\delta tof / \delta TOF$ is determined with an accuracy of < 0.5 % by use of a time-calibration pulse-generator. Hence, the absolute time-scale (eq. (3)) depends only on the constant TOF_o which can be determined from the curve tof (TOF) obtained by a linear regression analysis (fig. 30).

Evidently, there is a strong dependence of the resulting absolute time scale on the energy calibration as well as on the energy losses (Δe_i). It should be noted, however, that the energy losses within the target layer *do not influence* the calibration at all.

Aiming to check the consistency of this calibration procedure, a test measurement was carried out using a ^{252}Cf(sf) source. An additional transmission avalanche counter was mounted near the target position in order to generate the START-signal for the TOF measurement. (Else the timing reference signal is given by the RF of the cyclotron.) In this way the time calibration was performed by means of a TOF-TOF-analysis for the paired

fission fragments recorded by two opposite detector modules. The absolute time-scale deduced from the TOF-TOF-analysis agrees with the time calibration described above within 0.5 ÷1 ns.

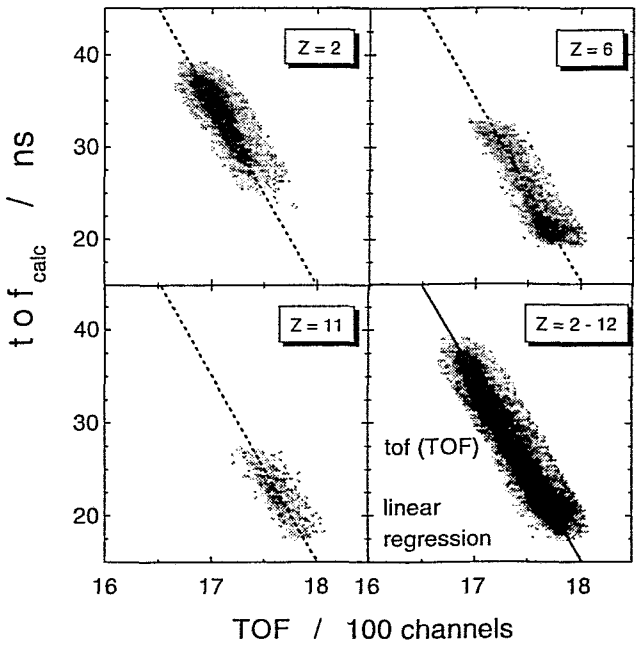

Fig. 30 Absolute calibration of the TOF-scale. The measured values (TOF) are compared with those calculated by eq. (2) (tof_{calc}) for selected events generated by particles with known parameters. A linear regression analysis delivers the curve tof (TOF) for the determination of the constant TOF_0 of eq. (3).

4.2 Calibration of the scintillation detectors

Since the total integrals of the light pulses of the CsI(Tl)-scintillators are not recorded, the energy calibration is performed by comparison of simulated and measured particle-identification branches (fig. 18) [40]. A model of a two-component pulse-shape L(t) for LCPs (eq. (4)) was normalized to the non-linear and particle-dependent response of CsI(Tl) (eq. (5)) [41],

$$L(t) = (h_{FAST}/\tau_{FAST}) \cdot \exp(-t/\tau_{FAST}) + (h_{SLOW}/\tau_{SLOW}) \cdot \exp(-t/\tau_{SLOW}) - (h_{FAST}/\tau_{FAST} + h_{SLOW}/\tau_{SLOW}) \cdot \exp(-t/\tau_{FRONT}) \quad (4)$$

$$L(E, Z, A) = S \cdot [E - a(Z,A) \cdot \ln(E/a(Z,A) + 1)] \quad (5)$$

where τ_i is the rise and decay time constant of the scintillation light pulse, respectively, h_i denotes the magnitude of the light components, S is the absolute scintillation efficiency, and a(Z,A) is a particle-dependent quenching constant.

Using appropriate empirical functions for the dependence of τ_{FAST} and of the ratio h_{SLOW} / h_{FAST} on the particle type (Z,A) and energy (E), and performing the integration of L(t) within the time gates (Δt_1 , Δt_2) a particle-identification matrix has been simulated (fig. 31a). The punch-through energies of protons, deuterons and tritons were used for adjusting the simulated to the measured particle-identification matrices. Additional normalization points are delivered by the tof-value of low-energy α-particles registered by the PSACs and stopped in the scintillators. The simulated particle-identification matrix then defines the absolute energy scales for all LCPs simultaneously [40] (fig. 31b).

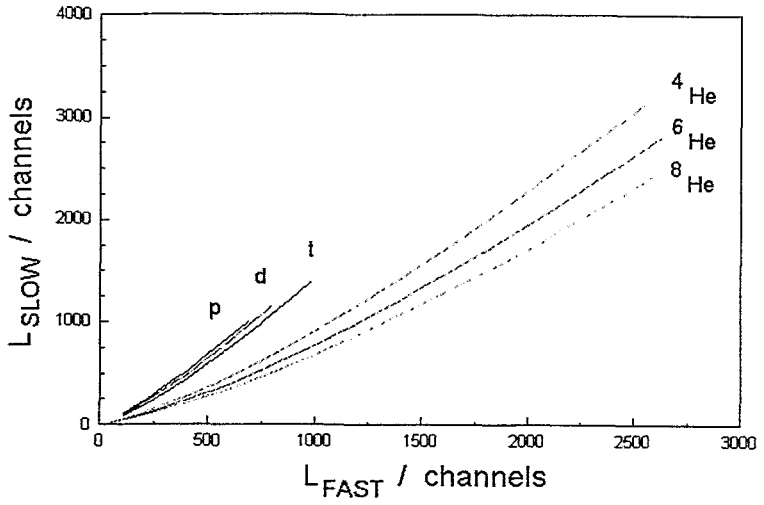

Fig. 31 Simulation of the particle branches of an LCP-identification matrix for CsI(Tl) as it follows from the application of the pulse-shape analysis method (upper panel).

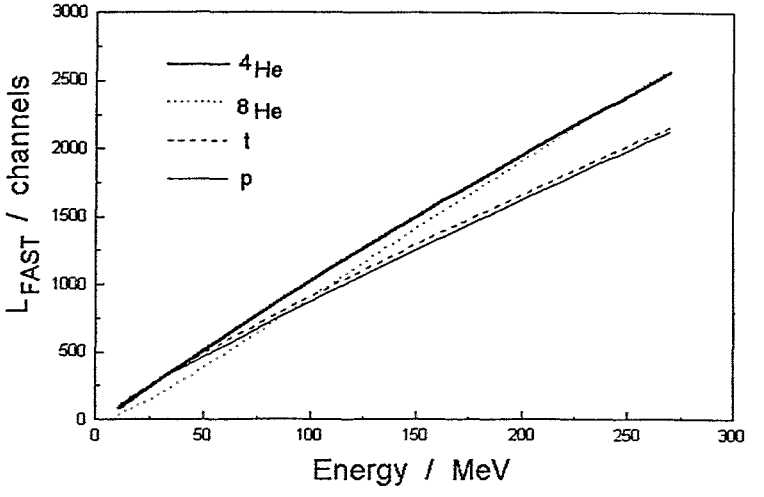

Energy-calibration curves for several LCP (lower panel).

The calibration of the phoswich detectors of the forward array has been described earlier in ref. [24].

5. PHYSICAL OBSERVABLES OF CHARGED PARTICLES

In the following we refer to a particle-oriented data set, where each individual fragment ($Z \geq 2$) is characterized by its calibrated parameters (ϑ, φ, tof, e_R). For a large amount of recorded IMF the fragment charge (Z) is additionally determined by Bragg-peak spectroscopy. It should be emphasized once more, that the applied calibration procedure *does not suppose any correlation between the fragments* registered in an event.

From the calibrated data further physical observables can be derived, namely the fragment masses (m), the primary emission energies (e), and, eventually, the velocity and linear momentum vectors (v, p). The main difficulties concerning m and e arise from the energy losses of the fragments in the (though very thin) detector foils. Since the energy loss, on the other hand, depends on Z and v, the mass determination requires to solve the following system of equations,

$$e_o(\text{tof}, A) = A/2 \cdot (d/\text{tof})^2 \tag{6}$$

$$e_o(e_R, A) = e_R + \sum_{i=1,k} \Delta e_i(e_o, Z(A), n_i) \tag{7}$$

where e_o is the kinetic energy of the fragment at the START-position of the TOF measurement. It is obvious that e_o influences both parameters tof and e_R. Concerning the fragments not identified by Z, a suitable A(Z)-relation has to be introduced into eqs. (6, 7). Since tof and e_R are fixed parameters, the solution of eqs. (6, 7) is of importance because of the following reasons:

(i) The effective thickness of the detector foils is a function of the PSAC coordinates (x,y). Additional uncertainties can be caused by non-planar surfaces and local nonuniformities.

(ii) The STOP-signal generated by the PSAC is position-dependent due to electronic signal delays.

(iii) The e_R-values have to be corrected for the energy loss by nuclear stopping not contained in E_R. This so-called ionization defect was evaluated for P-10 applying the method described in ref. [42]. For fission fragments these corrections amount to $2 \div 3$ MeV.

To solve eqs. (6, 7) an iterative procedure was developed [43]. For the processing of the extensive data sets as being typical for FOBOS experiments an acceleration of this procedure was achieved by dividing the task into several steps. This method is described below in detail.

In the first step, a set of tables is generated by means of a simulation code, which calculates a grid of (tof, e_R) - spot points for a given Z. The input data for the calculation of the Z(tof, e_R, F)-matrices are defined by the experimental conditions, i.e. the geometry of the set-up, the compositions of the detector materials (window foils, electrodes, gas-filled sections), and the thicknesses of the different layers, which are assumed to be parallel to each other and planar. The factor $F \geq 1$ (cf. eq. (8)) considers the position (i.e. angular) dependence of all distances and path lengths through the detector materials. The (x,y)-dependence is reduced due to the axial symmetry of the gas-filled detectors. The remaining parameter is the angle ε between the emission direction of the fragment (ϑ,φ) and the common normal of the detector layers. It is determined by eqs. (8, 9),

$$F(x,y) = 1 / \cos \varepsilon(x,y) \tag{8}$$

$$\tan^2 \varepsilon(x,y) = (x^2 + y^2) / L^2 \tag{9}$$

where L refers to the distance between the target and the plane of the entrance foil of the BIC.

Since the acceptance angle of the large gas-detector module corresponds to a maximal value $\varepsilon^{max} = 16.5\,^{\circ}$, the effective thickness of any layer penetrated by the fragments cannot increase more than 4.5 % with respect to the normal angle of incidence. Therefore, a relatively small number of spot-points within the limited range of F-values is enough to consider the (x,y)-dependence with sufficient accuracy.

The second step, the "event by event" determination of the mass m, is based on the calculated tables. Firstly, the F-value is deduced, and the tof is corrected for its electronic position dependence. By means of a two-dimensional interpolation between relevant spot-points of the tables, an interval [Z_1 (tof,e_R, F_1) , Z_2 (tof, e_R, F_2)] is determined for the fragment charge considering $F_1 < F < F_2$. The final result for Z is obtained from a linear interpolation with respect to F. Finally, the mass of the fragment can be deduced if the A(Z)-relation is given.

Since the energy losses ($\Sigma \Delta e_i$) can — in particular for FFs — exceed 50 % of the energy e_o, the preparation of sufficiently accurate energy-loss data turned out to be the most critical point for the mass determination. In fact, were calculated by use of the code STOPOW [39], which represents a modified version of the algorithm developed in ref. [44]. A detailed

analysis of the generated range-energy data set, however, indicated that the so-called Z1-oscillations, observed for fragments of large Z at keV-energies [45], are overestimated at energies of $E / A \leq 1$ MeV/A. This can also be observed in the e_R versus tof plot of fig. 32, which was calculated for given Z and A(Z) at F = const. Since different Z-branches in some areas may even overlap, an unambiguous solution of eqs. (6, 7) does not exist.

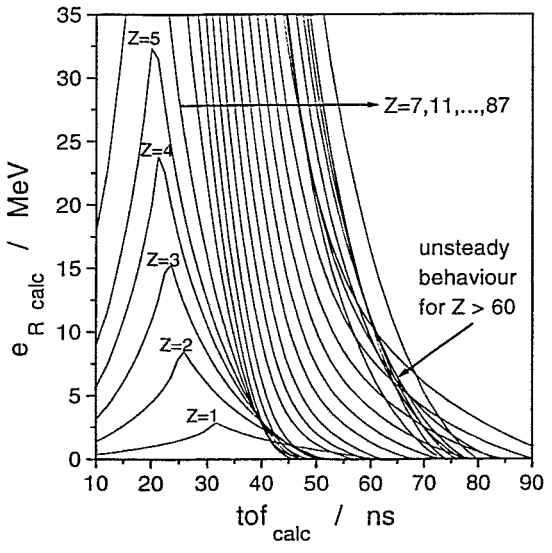

Fig. 32 Calculation of e_R versus tof for a gas-detector module. The lines correspond to different atomic numbers (Z) of the particles. The range-energy tables used for the determination of the energy losses were calculated by means of the code STOPOW88.

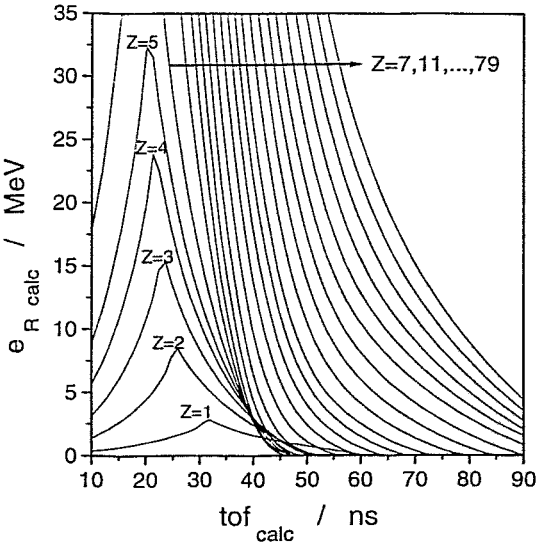

Fig. 33 The same calculation as shown in fig. 32, but by use of the modified range-energy data set (see text) for the calculation of the energy losses. The distance between the lines corresponding to increasing Z changes here smoothly.

Test measurements with a ^{252}Cf(sf) source were carried out to select FFs with known mean $<Z>$ and $<A>$. Consistency with the calculated e_R versus tof data was obtained for these ($< Z >$,$< A >$) by an appropriate modification of the original range-energy data set. Hence, the data for the remaining Z were deduced by a suitable interpolation. In this way, an "empirically improved" range-energy data set was generated and used for the calculation of the e_R versus tof plot shown in fig. 33. The relation Z(tof, e_R , A) is then unambiguous, likewise the solution of eqs. (6, 7). To check these modified range-energy data, the FF mass distribution determined from the ^{252}Cf(sf) measurement is compared in fig. 34 with reference data taken from ref. [46]. The peak of the light fragment is well reproduced, the maximumdeviation at the largest fragment masses is $\approx$ 7 a.m.u. A further analysis showed (see section 6.2.1), that this approach is even valid up to A $\approx$ 190.

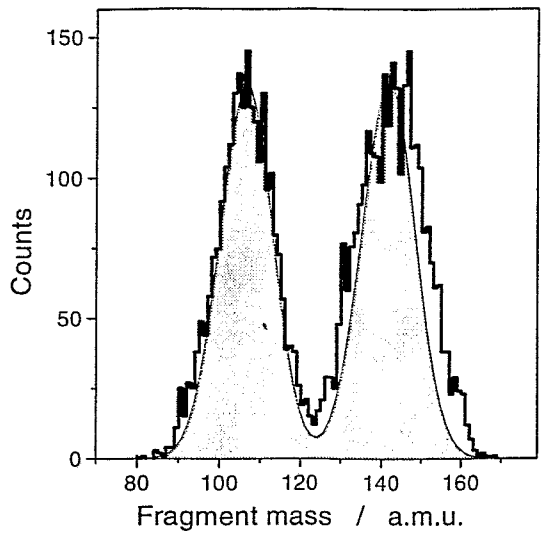

Fig. 34 Mass distribution of fission fragments (histogram) derived from a measurement with a ^{252}Cf(sf) source. For comparison, the single-mode Gaussian approximation for the mass distribution published in ref. [46] is shown (filled area). The spectra are normalized at the peak of the light fragment.

In the third step the primary emission energy e_o of the fragment (A,Z) is calculated assuming a mean value for the thickness of the target layer. The areal density of the target is known, but a mean value arises due to the different emission angles of the fragments with respect to the target normal. In principle, a procedure analogous to that applied for the mass determination could be developed with respect to e_o too. When calculating e_o (tof, e_R , x, y), however, the additional energy loss of the fragments within the target layer must be taken into account. In the general case, the target layer is positioned under a fixed angle, e.g., in relation to the beam axis. This distorts the axial symmetry of the experimental set-up. Therefore, the simple parametrization for F(x,y) (eqs. (8, 9)) is not yet valid, and a correct calculation would require a large number of prepared tables in dependence on the coordinates (x,y). For this reason, the *effective* target thickness and the corresponding energy losses have been evaluated "event by event". Considering a value for the ionization defect Def [e_o (A, Z, e_R)] as given in ref. [42], the fragment energy e_R (E_R) at the entrance into the gas volume of the BICs is used to simulate the history of the particle "backward" to the target. In this manner, both e_o and tof were calculated as described in section 4.1.3.

In the further analysis, the calculated tof is used to check the main condition for a correct determination of e_R , namely, that any calculated value must agree with the measured one if the fragment is stopped within the gas volume of the BIC. Otherwise, if the fragment passed through the BIC and lost there a sufficiently large amount of energy, the tof calculated for this fragment is expected to be significantly *larger* than the measured one. In this case, the e_R deduced from E_R is increased until the calculated tof agrees with the measured one. This last procedure enables to determine the e_o also for those fragments which penetrated the BIC (mainly light IMFs).

Finally, the linear momentum vectors (p_i) of all the fragments (i) emitted in one event can be obtained from the individual (ϑ, φ, v, A, Z). The accuracy of p is mass-dependent. It amounts to σ_p / p $\approx$ 3 % for FFs of ^{252}Cf(sf).

6. EXPERIMENTS AT FOBOS

In this chapter, some features of the actual performance of the spectrometer FOBOS are discussed. The main aim is more an illustration of the quality of measurements at low fragment multiplicities than the consequent derivation of physical results which are published elsewhere. With reference to a first series of experiments at FOBOS, several applications of this spectrometer are briefly treated.

6.1 Fragment spectroscopy of spontaneous fission

Considerable progress in detection techniques for FFs has been achieved in recent years, and high resolution data have been obtained for spontaneous fissioning nuclides. With the help of a twin ionization chamber (E-E-method [47]) single FF masses could be resolved in the cold fission region [48]. This method looses its outstanding performance for lower total kinetic energies (TKE) of the FFs because neutron emission affects the measured energies. (Every emitted neutron additionally deteriorates the mass determination of the FFs by approximately $\sigma_m \approx 1.5$ a.m.u. due to the recoil. Furthermore, prior-to-fission and post-fission neutron emission quantities are mixed in the analysis.)

Correlation measurements for pairs of FFs from spontaneous fission have been performed at the FOBOS spectrometer applying the TOF-TOF-method [49]. The START-signal was delivered by either a channel-plate detector or a transmission avalanche counter, and the STOP-signals were generated by the large-area PSACs. By operating several PSACs and correcting the position-dependence of the timing signals, the main drawback of most TOF measurements — their low geometrical efficiency — has been overcome. Although single masses were not resolved in the cold fission region, the TOF-TOF-method provides the following advantages, especially at lower TKE (cf. tab. 3), when comparing to the E-E-method:

(i) For nuclides with a low fission branch, e.g. ^{244}Cm(sf) ($1.5 \cdot 10^6$ α-particles per fission), sufficient statistics of FF coincidences can be easily collected, because the avalanche counters are able to discriminate up to 10^7 α-signals per second [50, 51]. At such rates, the E-E-method would fail due to the multiple pile-up of α-particle signals.

(ii) The FF quantities derived by the TOF-TOF-method are prior-to-neutron-emission ones which are more directly connected with the physical phenomena studied in such experiments.

(iii)The neutron emission affects the mass determination at least two times less than in the case of the E-E-method. Both methods essentially derive the FF mass ratio from the ratio of the measured quantities (eq. (10)) assuming momentum conservation

$$m_1 / m_2 = v_2 / v_1 = e_2 / e_1 . \qquad (10)$$

A certain relative change of a FF velocity component in flight direction ($\Delta v_i / v_i$) causes a relative change in the FF energy of $\Delta e_i / e_i = 2 \cdot \Delta v_i / v_i$.

Another source of errors in the E-E-method is absent in the TOF-TOF-method, namely, the dependence of the measured FF energy ratio on the sharing of the neutron emission between both fragments.

A well known problem of charged-particle spectroscopy is the occurrence of tails towards lower energy which are caused by scattering or impact on detector and constructional edges. This leads to a background of "wrong" events with too low TKE.

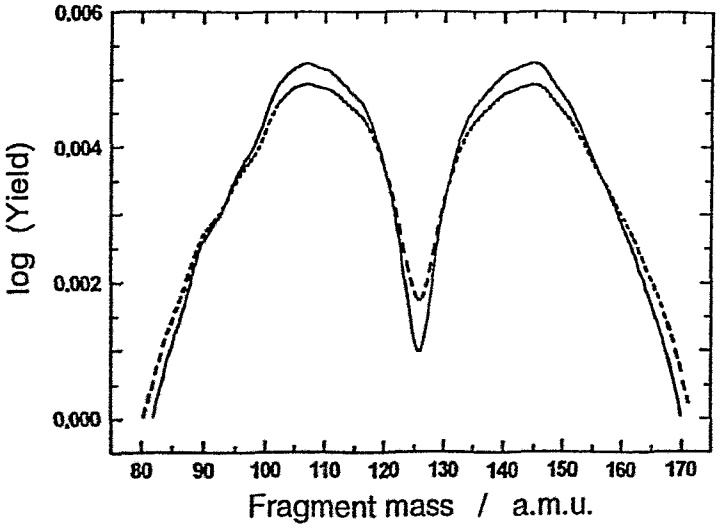

Fig. 35 Mass distribution of fission fragments of a ^{252} Cf(sf) source as measured by the TOF-TOF-method (dashed line: all events; full line: selected events; see text).

A considerable reduction of such a background has been achieved by combining the TOF-TOF-analysis with the independent fragment mass determination from tof and e_R (see chapter 5). Since in most of the distorted events only one fragment is affected, the sum of the linear momenta of both FFs deviates from zero. Therefore, the result obtained by the TOF-TOF-analysis differs from that based on tof and e_R. The events get ruled out, if the momentum sum derived from tof and e_R is larger than the experimental resolution ($\Delta p \approx \pm 200$ MeV/c), or if the difference of both results exceeds their uncertainties. With the help of such a check for consistency, the background at low TKE mentioned above can be suppressed (fig. 35). A value for the peak-to-valley ratio of 52 has been achieved in the FF mass distribution of ^{252}Cf(sf) [52].

6.2 Fragmentation of hot nuclei

6.2.1 TKE - Mass distributions of binary fission of hot nuclei

The TKE of the fragments is a measure of the Coulomb repulsion in the exit channel. It is closely connected with the geometrical and other conditions in a late state of the disintegration process. Since these conditions may change at high temperatures, one is interested in precise TKE-M data for the fission of hot nuclei.

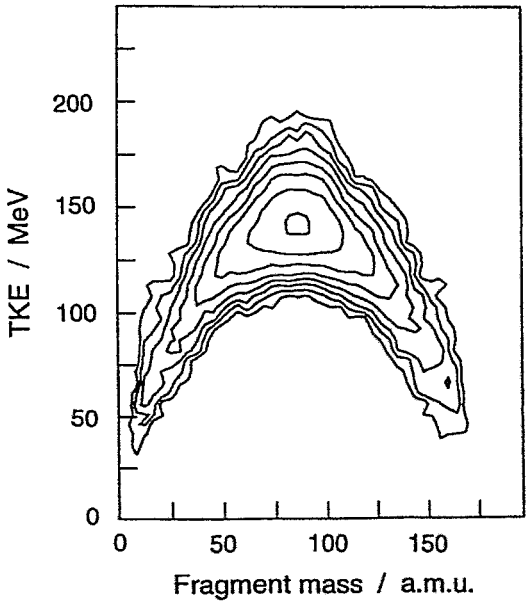

Fig. 36 TKE-M distribution of fragment pairs emitted in the reaction ^{14}N (34 AMeV) + ^{197}Au at large linear momentum transfer.

The well known classical tools, e.g. the kinematical coincidence method [53] which uses certain kinematical boundary conditions to derive the interesting quantities from the measured velocity vectors of the fragments, involve increasingly larger uncertainties, if the bombarding energy is increased. The reason is that the c.m. frame of the fragments in the output channel deviates more and more from the c.m. frame in the input channel due to the fluctuating incomplete momentum transfer in the early stage of reaction and due to fluctuations in the cascade of light-particle evaporation.

The additional information delivered by the FOBOS modules — both fragment masses at scission are determined independently from each other — allows one to derive both the TKE and the velocity vectors in the frame of the fissioning system. In this way, any processes which happened before scission do not affect the measured TKE-M distributions. Reconstructing the total transferred linear momentum (LMT) from the parameters p_i of all fragments in the collision and applying the massive transfer model [54], the excitation energy (E*) of the decaying system can be evaluated [55, 56]. Furthermore, the low registration thresholds of FOBOS allow to measure TKE-M distributions in a wide range of the fragment mass and to study their dependence on the LMT.

The TKE-M distribution of pairs of fragments emitted in the reaction ^{14}N (34 AMeV) + ^{197}Au at large LMT is shown in fig. 36. It is characterized by a large amount of symmetric fission and branches extending to very asymmetric mass splits. The mean TKE in dependence on the mass-asymmetry parameter was derived. Conclusions about energy dissipation and some confirmation of early theoretical predictions about an unique decay mechanism are given in ref. [57].

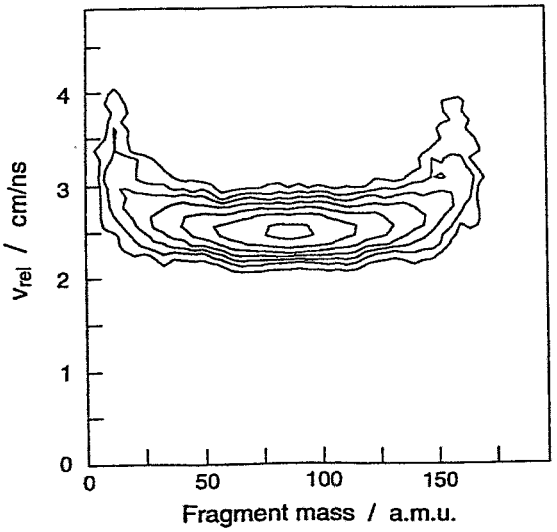

Fig. 37 Relative c.m. velocities (v_{rel}) between binary fragments emitted in the reaction ^{14}N (34 AMeV) + ^{197}Au.

The relative c. m. velocities (v_{rel}) between binary fragments from the reaction ^{14}N (34 AMeV) + ^{197}Au are given in fig. 37 in dependence on the mass number of one of the partners. The mean values for nearly symmetric disintegrations are in accordance with the systematics of ref. [58]. Deviations from a fission-like behavior were observed for very asymmetric binary decays. The larger v_{rel} should be connected with a more compact configuration at scission [57].

6.2.2 Velocity analysis of ternary decays

Hot nuclei with $E^* \leq 280$ MeV were produced in the reaction ^{7}Li (43 AMeV) + ^{232}Th [59]. On a yield level of ≈ 0.1 %, the dominating fission channel is competed with IMF-accompanied fission ($Z_{IMF} = 3 \div 8$) [60, 61], as already observed in ref. [62]. The third companion in fission can also be an α-particle [63].

The independent measurement of the fragment parameters in a 4π-geometry enables a velocity analysis with respect to the c. m. of the fissioning system. From both, FF masses and velocities, the frame of the fissioning system was derived, and the velocity of the third fragment was transformed into this frame. Two groups of particles with velocities above $v_{rel} = 2.5$ cm ns^{-1} and below $v_{rel} = 2.4$ cm ns^{-1}, respectively, are clearly distinguished in the reaction ^{14}N (34 AMeV) + ^{197}Au (fig. 38).

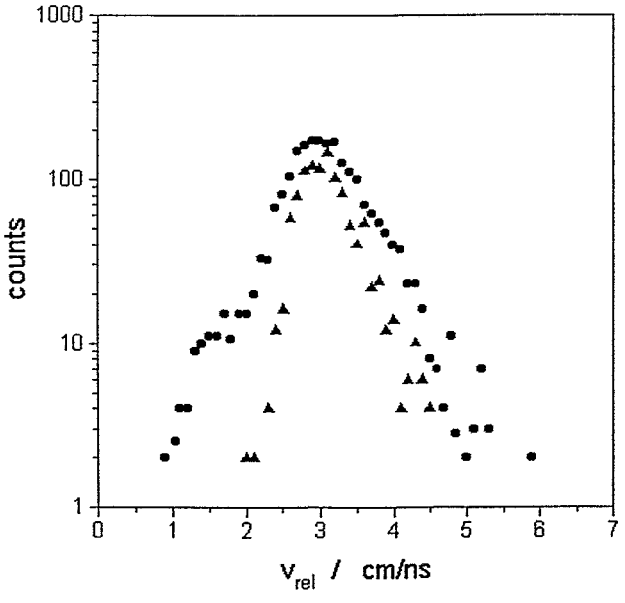

Fig. 38 Relative velocity (v_{rel}) distribution of fragments from binary and ternary decays of the composite system created in the reaction ^{14}N (34 AMeV) + ^{197}Au.
(full triangles: v_{rel} between fragment pairs in very asymmetric binary decays;
full circles: v_{rel} between the IMF accompanying fission and the c.m. of the fissioning system in ternary decays)

The different dependence on E^* of the yields of these two components [64] allows one to conclude that the high-energy component results from the emission of a hot compound-like nucleus, and the low-energy component arises from an emission during a later stage of the fission process near scission, where the system has a very deformed shape [65].

6.2.3 The charged-particle clock

Since the gas-filled detectors of FOBOS are not sensitive to LCPs, correlations of fragments with LCPs can be investigated within a 4π-geometry. Interesting possibilities are opened by the use of LCPs as a charged-particle clock for fission of hot nuclei [63, 66].

The principle of the adequate so-called neutron clock is described in ref. [67]. It is based on the discrimination of prior-to-scission- and post-scission-emitted neutron yields which are connected with the time evolution of the fission process and the corresponding loss of E* of the hot nucleus. Conclusions on the dynamics of the fission process [68, 69] can be made.

At temperatures of the composite system higher than $T \approx 3$ MeV, LCPs compete with neutrons in the evaporation cascade [70]. Although the neutron multiplicity is larger than the LCP multiplicity, LCPs are usually registered with a larger efficiency.

The effective solid angle of the scintillator shell of FOBOS ($\Delta\Omega_{CsI} \approx 4$ sr) allows for coincidence measurements with a high statistical accuracy enabling the study of the interplay of fission and LCP emission of hot nuclei. Correlations of LCPs with FFs have been analyzed for the reaction ^{14}N (53 AMeV) + ^{197}Au [60] to distinguish between different sources of LCP emission.

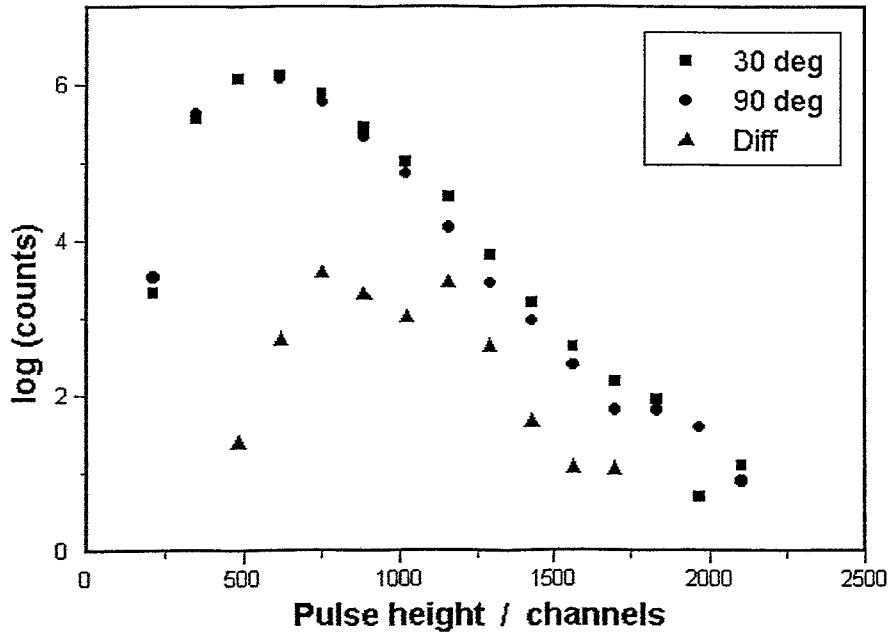

Fig. 39 The post-scission-emitted component of α-particles (full triangles) was separated from the prior-to-scission-emitted one by a correlation analysis of the α-accompanied fission in the reaction ^{14}N (53 AMeV) + ^{197}Au. The spectra of α-particles emitted at a mean angle of 30° and 90° with respect to the fission axis are indicated by full squares and full circles, respectively.

The post-scission-emitted component of α-particles could be separated from the prior-to-scission-emitted one by comparison of the spectra measured at different angles between the main fission axis and the direction of α-particle emission. Under certain kinematical conditions the post-scission-emitted component occurs at a larger mean energy than the prior-to-scission-emitted one (fig. 39).

The FOBOS spectrometer provides the means for a detailed study of, e.g., the dependence of the LCP components on the mass asymmetry of the disintegration, promising new insights on the dynamics of the fission process at large primary E*.

7. SUMMARY

The design, main measuring principles, detectors and service technique of the 4π-fragment-spectrometer FOBOS were described.

Particular attention has been paid to a detailed description of the calibration procedures developed, and to the derivation of physical observables from the measured values. The independent determination of the fragment parameters without any assumptions about the kinematics of the considered nuclear reaction plays a key-role for the investigation of the decay of hot nuclear systems produced by incomplete fusion.

The low registration thresholds and the broad dynamical range of the spectrometer make it a suitable tool for correlation measurements of charged reaction products in the Fermi-energy domain where low fragment multiplicities dominate.

The applied method of measurement has several advantages for the study of spontaneous fission.

Acknowledgments

We like to thank very much all the people who supported and helped us during the phase of design and construction of the FOBOS spectrometer, stimulated the development of this device in innumerable useful discussions, made the first series of experiment proposals, and, last but not least, the people that gave us technical assistance in solving the well-known everyday problems.

Especially, we would like to thank E.A. Cherepanov, G.G. Chubarian, B. Danziger, J. Fiedler, R. Förster, H. Freiesleben, H. Fuchs, F. Gleisberg, A. Gobbi, E. Grosse, H. Hartwig, D. Hilscher, J. Holik, J. Hutsch, G.F. Issayev, A.I. Ivanenko, W. Janczur, K.-H. Kaun, T. Kiehne, R. Kotte, J. Krüger, A.N. Mezentsev, E. Norbeck, H. Oeschler, J. Peter, H. Prade, M. Renz, A.V. Reshetov, G. Röpke, H. Schopper, H. Schunk, R.H. Siemssen, E.M. Smirnova, M. Sobiella, F. Stary, M. Di Toro, Ts.D. Vylov, D. Walzog, Th. Wilpert, D. Wohlfarth, R. Wolski, V.I. Zagrebaev, and Sh. S. Zeinalov.

We are indepted to the staff of the U-400M cyclotron of the FLNR Dubna for the outstanding co-operation during the experiments, especially to B.N. Gikal, G.G. Gulbekian, and V.B. Kutner.

The careful reading of the manuscript by F. Dönau is gratefully acknowledged.

Tables

Table 1 : Geometry of the FOBOS spectrometer in its normal position.

Ring	Module type	$<\vartheta>$	Module Nr.: $<\varphi>$				
exit	pentagon	0°					
1	hexagon	37.377°	1 : 90°	2 : 162°	3 : 234°	4 : 306°	5 : 18°
2	pentagon	63.435°	6 : 126°	7 : 198°	8 : 270°	9 : 342°	10: 54°
3	hexagon	79.187°	11: 90°	12: 162°	13: 234°	14: 306°	15: 18°
4	hexagon	100.813°	16: 126°	17: 198°	18: 270°	19: 342°	20: 54°
5	pentagon	116.565°	21: 90°	22: 162°	23: 234°	24: 306°	25: 18°
6	hexagon	142.623°	26: 126°	27: 198°	28: 270°	29: 342°	30: 54°
entrance	pentagon	180°					

Table 2 : Geometry of the FOBOS forward array.

Ring	Number of phoswich detectors	$<\vartheta>$
1	12	5°
2	16	8°
3	16	10.5°
4	16	14°
5	16	18.5°
6	16	23.5°

Table 3 : Uncertainties (1σ / a.m.u.) of the fragment mass determination for different neutron multiplicities.

Method	σ_m (0n)	σ_m (1n)	σ_m (4n)
E - E	< 0.2 [1]	1.5 [3]	3.5 [3]
TOF-TOF	0.4 [2]	0.7 [3]	1.4 [3]

[1] from cold fission spectra of ref. [48].

[2] from ^{252}Cf(sf) data taken at FOBOS [52].

[3] estimated value assuming a neutron kinetic energy of 2 MeV.

References

[1] H.-G. Ortlepp, M. Andrassy, G.G. Chubarian, M. Danziger, T. Dietterle, A.S. Fomichev, Sh.M. Heinitz, C.-M. Herbach, A.I. Ivanenko, I.V. Kolesov, D. May, Yu.Ts. Oganessian, Yu.E. Penionzhkevich, G. Renz, L.A. Rubinskaya, O.V. Strekalovsky, V.M. Vasko, W.D. Fromm, K. Heidel, H. Sodan, W. Wagner, B.A. Burova, S.V. Radnev, and I.D. Sandrev, Proc. of the Internat. Conf. on New Nuclear Physics with Advanced Techniques, Ierapetra, Crete, Greece, 1991 (Eds. F.A. Beck, S. Kossionides & C.A. Kalfas) World Scientific, Singapore, 1992, p. 302; Proc. of the Internat. Conf. on Exotic Nuclei, Foros, Crimea, Ukraine, 1991 (Eds. Yu.E. Penionzhkevich and R. Kalpakchieva) World Scientific, Singapore, 1992, p. 345.

[2] H.-G. Ortlepp, M. Andrassy, G.G. Chubarian, M. Danziger, P. Gippner, L. Dietterle, A.S. Fomichev, C.-M. Herbach, A.I. Ivanenko, I.V. Kolesov, A. Matthies, D. May, Yu.Ts. Oganessian, Yu.E. Penionzhkevich, V.N. Pokrovsky, G. Renz, L.A. Rubinskaya, O.V. Strekalovsky, V.V. Trofimov, V.M. Vasko, K. Heidel, K.D. Schilling, W. Seidel, H. Sodan, W. Wagner, V.E. Zhuchko, H. Fuchs, D. Hilscher, H. Homeyer, P. Ziem, G. Pausch, B.A. Burova, S.V. Radnev, and I.D. Sandrev, Proc. of the Internat. School-Seminar on Heavy Ion Physics, Dubna, Russia, 1993 (Eds. Yu.Ts. Oganessian, Yu.E. Penionzhkevich, and R. Kalpakchieva) JINR E7-93-274, Dubna, 1993, vol. 2, p. 466; Proc. of the FOBOS workshop '94, Cracow, Poland, 1994 (Ed. W. Wagner) FZR-65, Rossendorf, Germany, 1995, p. 29; M. Andrassy, A.A. Aleksandrov, I.A. Aleksandrova, A. Budzanowski, M. Danziger, L. Dietterle, V.N. Doronin, S. Dshemuchadse, A.S. Fomichev, P. Gippner, M. Gebhardt, K. Heidel, Sh. Heinitz, C.-M. Herbach, D. Hilscher, J. Holik, H. Homeyer, A.I. Ivanenko, S.A. Ivanovsky, W. Janczur, D.V. Kamanin, I.V. Kolesov, A. Matthies, D. May, S.I. Merzlyakov, W. von Oertzen, Yu.Ts. Oganessian, H.-G. Ortlepp, G. Pausch, Yu.E. Penionzhkevich, V.N. Pokrovsky, Yu.V. Pyatkov, S.V. Radnev, G. Renz, L.A. Rubinskaya, I.D. Sandrev, K.D. Schilling, W. Seidel, D.I. Shishkin, H. Sodan, O.V. Strekalovsky, V.V. Trofimov, I.P. Tsurin, C. Umlauf, D.V. Vakatov, V.M. Vasko, W. Wagner, V.E. Zhuchko, P. Ziem, and L. Zrodlowski, JINR E7-95-148, Dubna, Russia, 1995.

[3] E. Will, H. Sodan, I.V. Kolesov, R. Kupchak, Yu.E. Penionzhkevich, Yu.Ts. Oganessian, and W. Seidel, Contr. at the Symp. on Experiments on Heavy Ion Beams, Varna, Bulgaria, 1984, JINR D7-84-736, Dubna, 1984, p. 70; H. Sodan, I.V. Kolesov, Yu.Ts. Oganessian, Yu.E. Penionzhkevich, D.Walzog, W. Seidel, R. Kotte, H.-G. Ortlepp, F. Stary, B.A. Burova, R.G. Kalpakchieva, S.V. Radnev, and I.V. Sandrev, Proc. of the Internat. School-Seminar on Heavy Ion Physics, JINR Dubna, 1986; A.G. Akhperdzanian, B.A. Burova, D. Walzog, W. Seidel, H. Sodan, R.G. Kalpakchieva, I.V. Kolesov, R. Kotte, Yu.Ts. Oganessian, H.-G. Ortlepp, Yu.E. Penionzhkevich, S.V. Radnev, I.D. Sandrev, F. Stary, A.S. Fomichev, and G.G. Chubarian, JINR P13-87-760, Dubna, 1987.

[4] G.N. Flerov, Yu.Ts Oganessian, S.L. Bogomolov, B.N. Gikal, G.G. Gulbekian, A.I. Ivanenko, V.V. Kamanin, B.A. Klenin, S.I. Kozlov, I.V. Kolesov, V.B. Kutner, V.N. Melnikov, E.A. Minin, A.M. Morduyev, P.Ts. Oganessian, A.S. Pasyuk, Yu.E. Penionzhkevich, K.I. Semin, B.V. Fefilov, and V.A. Chugreev, JINR 9-84-555, Dubna, 1984.

[5] S. Biri, A.A. Efremov, and V.B. Kutner, in: "Heavy Ion Physics", Scientific Report 1989/90 (Ed. B.I. Pustylnik) JINR E7-91-75, Dubna, Russia, 1991, p. 208.

[6] Yu.Ts. Oganessian and Yu.E. Penionzhkevich, JINR E7-94-245, Dubna, Russia, 1994.

[7] W. Wagner, A.S. Fomichev, C.-M. Herbach, A. Matthies, H.-G. Ortlepp, G. Pausch, O.V. Strekalovsky, and V.A. Vitenko, in: "Heavy Ion Physics", Scientific Report 1991/92 (Ed. B.I. Pustylnik) JINR E7-93-57, Dubna, Russia, 1993, p. 244; W. Wagner, A.S. Fomichev, H.-G. Ortlepp, C.-M. Herbach, A. Matthies, G. Pausch, O.V. Strekalovsky, M.A. Milovidov, and V.A.Vitenko, JINR Rapid Comm. 4 [61]-93, Dubna, Russia, 1993, p. 49.

[8] W. Wagner, H.-G. Ortlepp, D.V. Kamanin, A. Matthies, O.V. Strekalovsky, and V.E. Zuchko, Proc. of the FOBOS workshop '94, Cracow, Poland, 1994 (Ed. W. Wagner) FZR-65, Rossendorf, Germany, 1995, p. 40;

A.S. Fomichev, H.-G. Ortlepp, Yu.E. Penionzhkevich, C.-M. Herbach, I. David, W. Wagner, G. Pausch, H. Sodan, and V.A. Vitenko, JINR P15-92-50, Dubna, Russia, 1992.

[9] G.D. Westfall, J.E. Yurkon, G. Van der Plicht, Z.M. Koenig, B.V. Jacak, R. Fox, G.M. Crawley, M.R. Maier, B.E. Hasselquist, R.S. Tickle, and D. Horn, Nucl. Instr. and Meth. A238 (1985) 347.

[10] S.V. Radnev, I.D. Sandrev, B.D. Burova, Ch.K. Patchadshiev, Ts.R. Predov, and S.G. Gentchev, Contr. at the Internat. Conf. on Set-up FOBOS, Sofia, Bulgaria, 1990, JINR D7-90-539, Dubna, Russia, 1990, p. 17.

[11] W. Seidel, H.-G. Ortlepp, F. Stary, and H. Sodan, Nucl. Instr. and Meth. A273 (1988) 536.

[12] J. Pouthas, B. Borderie, R. Dayras, E. Plagnol, M.F. Rivet, F. Saint-Laurent, J.C. Steckmeyer, G. Auger, C.O. Bacri, S. Barbey, A. Barbier, A. Benkirane, J. Benlliure, B. Berthier, E. Bougamont, P. Bourgault, P. Box, R. Bzyl, B. Cahan, Y. Cassagnou, D. Charlet, J.L. Charvet, A. Chbihi, T. Clerc, N. Copinet, D. Cussol, M. Engrand, J.M. Gautier, Y. Huguet, O. Jouniaux, J.L. Laville, P. Le Botlan, A. Leconte, R. Legrain, P. Lelong, M. Le Guay, L. Martina, C. Mazur, P. Mosrin, L. Olivier, J.P. Passerieux, S. Pierre, B. Piquet, E. Plaige, E.C. Pollacco, B. Raine, A. Richard, J. Ropert, C. Spitaels, L. Stab, D. Sznajderman, L. Tassan-got, J. Tillier, M. Tripon, P. Vallerand, C. Volant, P. Volkov, J.P. Wieleczko, and G. Wittwer, Nucl. Instr. and Meth. A357 (1995) 418.

[13] C.R. Grun, M. Bimini, R. Legrain, R. Loveman, W. Pang, M. Roach, D.K. Scott, A. Shotter, T.J. Symons, J. Wouters, M. Zisman, R. de Vries, Y.C. Peng, and W. Sondersheim, Nucl. Instr. and Meth. 196 (1982) 33.

[14] A. Matthies, W. Seidel, R. Kotte, and H.-G. Ortlepp, Contr. at the Symp. on Correlation Experiments on Heavy Ion Beams, Dresden, 1988, JINR D7-88-299, Dubna, 1988, p. 11.

[15] O. Buneman, T.E. Granshaw, and J.A Harvey, Can. Journ. Res. A27 (1949) 191.

[16] H.-G. Ortlepp and A. Romaquera, Nucl. Instr. and Meth. A267 (1989) 500.

[17] A.A. Aleksandrov, I.A. Aleksandrova, L. Dietterle, V.N. Doronin, S. Dshemuchadse, P. Gippner, C.-M. Herbach, S.A. Ivanovsky, D.V. Kamanin, A. Matthies, D. May, H.-G. Ortlepp, G. Pausch, Yu.E. Penionzhkevich, G. Renz, K.D. Schilling, D.I. Shishkin, O.V. Strekalovsky, V.V. Trofimov, I.P. Tsurin, C. Umlauf, D.V. Vakatov, V.M. Vasko, W. Wagner, and V.E. Zhuchko, in: "Heavy Ion Physics", Scientific Report 1993/94 (Ed. B.I. Pustylnik) JINR E7-95-227, Dubna, Russia, 1995, p. 211.

[18] G. Renz, E. Will, W. Seidel, D. Walzog, and H.-G. Ortlepp, Contr. at the Symp. on Correlation Experiments on Heavy Ion Beams, Dresden, 1988, JINR D7-88-299, Dubna, 1988, p. 17.

[19] G. Renz, V.M. Vasko, P. Gippner, A. Matthies, V.N. Doronin, D.I. Shishkin, C. Umlauf, and M. Gebhardt, Proc. of the FOBOS workshop '94, Cracow, Poland, 1994 (Ed. W. Wagner) FZR-65, Rossendorf, Germany, 1995, p. 46; G. Renz , V.M. Vasko, P. Gippner, A. Matthies, V.N. Doronin, D.I. Shishkin, C. Umlauf, and M. Gebhardt, FZR-78, Rossendorf, Germany, 1995, p. 115; G. Renz, V.M. Vasko, P. Gippner, A. Matthies, V.N. Doronin, D.I. Shishkin, C. Umlauf, and M. Gebhardt, in: "Heavy Ion Physics", Scientific Report 1993/94 (Ed. B.I. Pustylnik) INR E7-95-227, Dubna, Russia, 1995, p. 222.

[20] M. Gebhardt, Diploma Thesis, Johann Wolfgang Goethe - Universität, Frankfurt am Main, Germany, 1995; M. Gebhardt, V.N. Doronin, P. Gippner, H.-G. Ortlepp, G. Renz, D.I. Shishkin, and W. Wagner, FZR-78, Rossendorf, Germany, 1995, p. 81.

[21] O.V. Strekalovsky, K. Heidel, S.I. Ivanovsky, D. May, H.-G. Ortlepp, G. Pausch, G. Renz, V.E. Zhuchko, W. Wagner, V.V. Trofimov, and I.P. Tsurin, Proc. of the XVI Internat. Symp. on Nuclear Electronics and VI Internat. School on Automation and Computing in Nuclear Physics and Astrophysics, Varna, Bulgaria, 1994 (Ed. I.N. Churin) JINR D13-94-491, Dubna, Russia, 1995, p. 31 O.V. Strekalovsky, K. Heidel, S.I. Ivanovsky, D. May, H.-G. Ortlepp, G. Pausch, G. Renz, V.V. Trofimov, I.P. Tsurin, W. Wagner, and V.E. Zhuchko, Proc. of the FOBOS workshop '94, Cracow, Poland, 1994 (Ed. W. Wagner) FZR-65, Rossendorf, Germany, 1995, p. 49.

[22] J. Alarja, A. Dauchy, A. Giorni, C. Morand, E. Pollaco, P. Stassi, R. Billerey, B. Chambon, B. Cheynis, D. Drain, and C. Pastor, Nucl. Instr. and Meth. A 242 (1986) 352.

[23] F. Benrachi, B. Chambon, B. Cheynis, D. Drain, C. Pastor, D. Seghier, K. Zaid, A. Giorni, D. Heuer, A. Llères, C. Morand, P. Stassi, and J.B. Viano, Nucl. Instr. and Meth. A281 (1989) 137.

[24] W. Terlau, PhD Thesis, Freie Universität Berlin, Germany, 1988.

[25] J. Tõke, S.A. Masserant, S.P. Baldwin, B. Lott, W.U. Schröder, and X. Zhao, UR-NSRL-394, University of Rochester, USA, 1993.

[26] P. Ziem, T. Kiehne, L. Dietterle, and V.V. Trofimov, FZR-92-11, Rossendorf, Germany, 1992, p. 19.

[27] STRUCK - Product Summary, Hamburg, Germany, 1990.

[28] C.A.E.N. - General Catalogue, Viareggio, Italy,1993.

[29] LeCroy - Research Instrumentation Catalog, Chestnut Ridge NY, USA, 1992.

[30] C.-M. Herbach and C. Umlauf, in: "Heavy Ion Physics", Scientific Report 1991/92, (Ed. B.I. Pustylnik) JINR E7-93-57, Dubna, Russia, 1993, p.250.

[31] G. Röschert, HMI-B436, Berlin, Germany, 1986; G. Röschert, "HOOPSY under VMS - A Program System for Multi-Parameter-Experiments", Version 12, Hahn-Meitner-Institut, Berlin, Germany, 1992.

[32] K.-P. Eckert, S. Gipp, and S. Wasserroth, HMI-D/M 154, Berlin, Germany, 1984; "OLYMP - A System for the Evaluation of multi- dimensional experimental Data and Spectra", Version 5.4, Hahn-Meitner-Institut, Berlin, Germany, 1992.

[33] C.-M. Herbach and D.V. Vakatov, Proc. of the FOBOS workshop '94, Cracow, Poland, 1994 (Ed. W. Wagner) FZR-65, Rossendorf, Germany, 1995, p. 56.

[34] B. Stroustrup, "The C++ Programming Language", Addison-Wesley, 1986.

[35] D.A. Young, "Object-Oriented Programming with C++ and OSF / MOTIF", Prentice Hall, 1992.

[36] M.I. Belyakov, Yu.I. Rabover, and A.L. Fridman, "The Portable Operational System", Radio i Svyaz, Moscow, Russia, 1991. (in Russian)

[37] H. Stelzer, "CAMDA - a CAMAC-PC Data Aquisition System", Messel, Germany, 1989.

[38] Ch. Schulz, Diploma Thesis, Technische Universität Berlin, Germany, 1995.

[39] J. Henninger and B. Horlbeck, JINR E6-84-366, Dubna, Russia,1984.

[40] W. Wagner and D.V. Kamanin, FZR-130, Rossendorf, Germany, 1996, p. 150.

[41] D. Horn, G.C. Ball, A. Galindo-Uribarri, E. Hagberg, R.B. Walker, R. Laforest, and J. Pouliot, Nucl. Instr. and Meth. A320 (1992) 273;
A.S. Fomichev, I. David, S.M. Lukyanov, Yu.E. Penionzhkevich, N.K. Skobelev, O.B. Tarasov, A. Matthies, H.-G. Ortlepp, W. Wagner, M. Lewitowicz, M.G. Saint-Laurent, J.M. Corre, Z. Dlouhy, I. Pecina, and C. Borcea, Nucl. Instr. and Meth. A344 (1994) 378.

[42] S. Kahlbitzer, H. Oetzmann, H. Grahmann, and A. Feuerstein, Z. Phys. A278 (1976) 233.

[43] C.-M. Herbach and H.-G. Ortlepp, in: "Heavy Ion Physics", Scientific Report 1991/92 (Ed. B.I. Pustylnik) JINR E7-93-57, Dubna, Russia, 1993, p. 253.

[44] J.F. Ziegler, "Handbook of Stopping Cross-Sections for Energetic Ions in All Elements", Pergamon Press, New York, 1980.

[45] J.H. Ormrod, J.R. Macdonald, and H.E. Duckworth, Can. Journ. Phys. 43 (1965) 275.

[46] R. Schmidt and H. Henschel, Nucl. Phys. A395 (1983) 15.

[47] C. Budtz-Jørgensen, H.-H. Knitter, Ch. Straede, F.-J. Hambsch, and R. Vogt, Nucl. Instr. and Meth. A258 (1987) 209.

[48] H.-H. Knitter, F.-J. Hambsch, and C. Budtz-Jørgensen, Nucl. Phys. A536 (1992) 221.

[49] Yu.V. Pyatkov, A.A. Aleksandrov, I.A. Aleksandrova, B.I. Andreev, P. Gippner, C.-M. Herbach, E.M. Kozulin, A. Matthies, Yu.Ts. Oganessian, H.-G. Ortlepp, Yu.E. Penionzhkevich, G. Renz, K.D. Schilling, O.V. Strekalovsky, V.M. Vasko, and W. Wagner,
Proc of the Internat. Workshop on Nuclear Fission and Fission Product Spectroscopy, Château de la Baume, Seyssins, France, 1994 (Eds. H. Faust & G. Fioni) Grenoble, 1994, p. 144.

[50] Yu.V. Pyatkov, A.A. Aleksandrov, B.I. Andreev, P. Gippner, C.-M. Herbach, H.-G. Ortlepp, Yu.E. Penionzhkevich, R.A. Shekhmamet'ev, and W. Wagner, FZR-98, Rossendorf, Germany, 1995.

[51] A.A. Aleksandrov, B.I. Andreev, P. Gippner, C.-M. Herbach, E.M. Kozulin, A. Matthies, Yu.Ts. Oganessian, H.-G. Ortlepp, Yu.E. Penionzhkevich, Yu.V. Pyatkov, G. Renz, K.D. Schilling, O.V. Strekalovsky, V.M. Vasko, and W. Wagner, FZR-99, Rossendorf, Germany, 1995.

[52] Yu.V. Pyatkov, V.V. Pashkevich, Yu.E. Penionzhkevich, V.G. Tishchenko, A.V. Unzhakova, H.-G. Ortlepp, P. Gippner, C.-M. Herbach, and W. Wagner, Proc. of the 3^{d} Internat. Conf. on Dynamical Aspects of Nuclear Fission, Casta-Papiernicka, Slovak Republic, 1996. (in print)

[53] A. Gobbi and W. Nörenberg, in: "Heavy Ion Collisions" (Ed. R. Bock) North-Holland, Amsterdam, 1980, vol. 2, p. 128;
W.U. Schroeder and J.R. Huizenga, in: "Treatise on Heavy-ion Science" (Ed. D.A. Bromley) Plenum Press, New York, 1984, vol. 2, p. 115;
G. Casini, P.R. Maurenzig, A. Olmi, and A.A. Stefanini, Nucl. Instr. and Meth. A277 (1989) 445.

[54] D. Guerreau, GANIL P89-07, Caen, France, 1989;
L.G. Moretto and G.J. Wozniak, in: "Progress in Particle and Nuclear Physics" (Ed. A. Faessler) Pergamon Press, New York, 1988, vol. 21, p. 401.

[55] C.-M. Herbach,
Proc. of the FOBOS workshop '94, Cracow, Poland, 1994 (Ed. W. Wagner) FZR-65, Rossendorf, Germany, 1995, p. 87.

[56] H.-G. Ortlepp, W. Wagner, A.A. Aleksandrov, I.A. Aleksandrova, L. Dietterle, V.N. Doronin, P. Gippner, C.-M. Herbach, S.A. Ivanovsky, D.V. Kamanin, A. Matthies, G. Pausch, Yu.E. Penionzhkevich, G. Renz, K.D. Schilling, D.I. Shishkin, O.V. Strekalovsky, V.V. Trofimov, I.P. Tsurin, C. Umlauf, D.V. Vakatov, V.M. Vasko, and V.E. Zhuchko,
in: "Low Energy Nuclear Dynamics" (Eds. Yu. Oganessian, W.von Oertzen, and R. Kalpakchieva) World Scientific, Singapore, 1995, p. 231.

[57] W. Wagner, H.-G. Ortlepp, P. Gippner, and C.-M. Herbach,
in: "Advances in Nuclear Dynamics 2 " (Eds. W. Bauer and G.D. Westfall) Plenum Press, New York, 1996, p. 341.

[58] V.E. Viola, Jr., Nucl. Data Sect. A1 (1966) 391;
V.E. Viola, K. Kwiatkowski, and M. Walker, Phys. Rev. C31 (1985) 1550.

[59] A.A. Aleksandrov, I.A. Aleksandrova, M. Andrassy, L. Dietterle, V.N. Doronin, P. Gippner, C.-M. Herbach, D. Hilscher, S.A. Ivanovsky, A. Matthies, D. May, H.-G. Ortlepp, G. Pausch, Yu.E.Penionzhkevich, V.N. Pokrovsky, G. Renz, K.D. Schilling, D.I. Shishkin, O.V. Strekalovsky, V.V. Trofimov, C. Umlauf, V.M. Vasko, D.V. Vakatov, W. Wagner, and V.E. Zhuchko, Nucl. Phys. A583 (1994) 465c.

[60] W. Wagner, H.-G. Ortlepp, C.-M. Herbach, P. Gippner, D.V. Kamanin, A. Matthies, Yu.E. Penionzhkevich, G. Renz, K.D. Schilling, O.V. Strekalovsky, D.V. Vakatov, and V.E. Zhuchko, Proc. of the 2^{d} Internat. Symp. on Heavy Ion Physics and its Applications, Lanzhou, China, 1995 (Eds. Y.X. Luo, G.M. Jin and J.Y. Liu) World Scientific, Singapore, 1996, p. 217; FZR-104, Rossendorf, Germany, 1995.

[61] W. Wagner, H.-G. Ortlepp, C.-M. Herbach, P. Gippner, A. Matthies, G. Pausch, Yu.E. Penionzhkevich, G. Renz, K.D. Schilling, O.V. Strekalovsky, and V.E. Zhuchko, Contr. to the Internat. Nuclear Physics. Conference, Beijing, China, 1995, China Institute of Atomic Energy, 1995, p. 5.5-7; FZR-105, Rossendorf, Germany, 1995.

[62] D.E. Fields, K. Kwiatkowski, K.B. Morley, E. Renshaw, J.L. Wile, S.J. Yennello, V.E. Viola, and R.G. Korteling, Phys. Rev. Lett. 69 (1992) 3713.

[63] K. Siwek-Wilczynska, J. Wilczynski, H.K.W. Leegte, R.H. Siemssen, H.W. Wilschut, K. Grotowski, A. Panasiewicz, Z. Sosin, and W. Wieloch, Phys. Rev. C48 (1993) 228.

[64] C.-M. Herbach, H.-G. Ortlepp, P. Gippner, K.D. Schilling, and W. Wagner, FZR-130, Rossendorf, Germany, 1996, p. 89.

[65] C.-M. Herbach, H.-G. Ortlepp, P. Gippner, D.V. Kamanin, Yu.E. Penionzhkevich, G. Renz, K.D. Schilling, O.V. Strekalovsky, V.G. Tichenko, and W. Wagner, Proc. of the Internat. Research Workshop - "Heavy Ion Physics at Low, Intermediate and Relativistic Energies Using 4π Detectors - 1996", Poiana Brasov, Romania, 1996 (Ed. M. Petrovici) World Scientific, Singapore. (in print)

[66] J.P. Lestone, J.R. Leigh, J.O. Newton, D.J. Hinde, J.X. Wei, J.X. Chen, S. Elfström, and M. Zielinska-Pfabe, Nucl. Phys. A559 (1993) 277.

[67] D.J. Hinde, D. Hilscher, H. Rossner, B. Gebauer, M. Lehmann, and M. Wilpert, Phys. Rev. C45 (1992) 1229;
D.J. Hinde, Nucl. Phys. A553 (1993) 255c;
D. Hilscher and H. Rossner, Ann. Phys. Fr. 22 (1992) 471.

[68] K. Siwek-Wilczynska, J. Wilczynski, R.H. Siemssen, and H.W. Wilschut, Nucl. Phys. A583 (1995) 141.

[69] D. Hilscher, in: "Low Energy Nuclear Dynamics" (Eds. Yu. Oganessian, W. von Oertzen, and R. Kalpakchieva) World Scientific, Singapore, 1995, p. 169.

[70] H. Delagrange, C. Gregoire, F. Scheuter, and Y. Abe, Z. Phys. A323 (1986) 437.